COMPARISON OF TRAVELING WAVE AND GAIN-CLAMPED SEMICONDUCTOR OPTICAL AMPLIFIERS
AND
IMPACT OF DISPERSION ON HYBRID OF FREQUENCY-HOPPED OPTICAL CDMA AND WDMA NETWORKS

COMPARISON OF TRAVELING WAVE AND GAIN-CLAMPED SEMICONDUCTOR OPTICAL AMPLIFIERS AND IMPACT OF DISPERSION ON HYBRID OF FREQUENCY-HOPPED OPTICAL CDMA AND WDMA NETWORKS

BY

KEVIN KE ZHANG, M.Eng. (Electrical)

AUGUST 2006

A THESIS

SUBMITTED TO THE DEPARTMENT OF ELECTRICAL AND COMPUTER ENGINEERING

AND THE COMMITTEE ON GRADUATE STUDIES

OF MCMASTER UNIVERSITY

IN PARTIAL FULFILLMENT OF THE REQUIREMENTS FOR THE DEGREE OF

MASTER OF APPLIED SCIENCE

MASTER OF APPLIED ŚCINCE (2006) McMASTER UNIVERSITY

(Electrical and Computer Engineering) Hamilton, Ontario

TITLE: **COMPARISON OF TRAVELING WAVE AND GAIN-CLAMPED SEMICONDUCTOR OPTICAL AMPLIFIERS**

AND

IMPACT OF DISPERSION ON HYBRID OF FREQUENCY-HOPPED OPTICAL CDMA **AND** WDMA **NETWORKS**

AUTHOR: Kevin Ke Zhang, M.Eng. (Xidian University, P. R. China)

SUPERVISOR: Dr. Wei-ping Huang

NUMBER OF PAGES : x,100

Abstract

(This thesis consists of two parts.)

Part I Comparison of Traveling Wave and Gain-Clamped Semiconductor Optical Amplifiers

Today's Wavelength Division Multiplexing (WDM) optical networks are getting dynamic light-path reconfigurable and optical transparent. Optical amplification without optoelectronic conversion is a key technology in all-optical networks. Semiconductor optical amplifier (SOA) is a very potential device in this field. Besides the linear amplification, the nonlinear features of SOA make it has a broad application in wavelength conversion, tunable wavelength filter, optical switching and optical logic. The simple structure and very compact size of SOA indicate the essential low-cost and compatibility of integration. Resonant cavity is the basic structure of conventional SOAs, while gain-clamped SOAs (GC-SOAs) provide a constant gain which raises a lot of interests in applications. SOA with Distributed Bragg Reflectors (DBR) is one of the structures to realize the clamped gain.

In this thesis the performances of traveling wave SOA (TW-SOA) and DBR-SOA are compared through a dynamic model. This model consists of a distributed feedback wave equation, a carrier rate equation and a material gain model, thereby can be used to simulate both of the two SOAs. To balance the time cost of simulation and the accuracy of the result, three important non-physical parameters, simulated bandwidth, cavity discritization and frequency discretizaiton, are investigated. The simulation results show that DBR-SOA has a very stable device gain which is independent on input optical power. From a noise level point of view DBR-SOA and TW-SOA have different characteristics. These comparison is conducted with both large signal input and small signal input.

In addition, a desirable application, SOA in a multi-channel WDM system, is also simulated with GC-SOA and TW-SOA. The Bit Error Rate (BER) of TW-SOA increases greatly due to inter-channel cross talk, while the BER of GC-SOA is virtually constant with the variation of WDM channel number. Another application, wavelength converter, shows TW-SOA is very useful in non-linear application.

Part II Impact of Dispersion on Hybrid of Frequency-Hopped Optical CDMA and WDMA Networks

A new analytical formula for analysis of the system performance of the Hybrid of Wavelength Division Multiple Access (WDMA) and Code Division Multiple Access (CDMA) is developed and presented. The effects of fiber dispersion and inter-channel crosstalk are considered and their impact on system performance is analyzed in terms of power penalty. Finally, methods to overcome the effects of the fiber dispersion are discussed.

Acknowledgement

First, I would like to sincerely thank my supervisor Dr. Weiping Huang for his encouragement, guidance, and support throughout my whole research process.

Second, I would also like to acknowledge Dr. Xun Li for many enlightening discussions in this work.

Third, I am very much grateful to the friendship and support from the staff and graduate students of Communications Research Lab for their valuable discussion in my study and life, especially acknowledging Dr. Xingzhong Chen, Dr. Genxiang Chen, Dr. Linping Shen, Jiang Zhu, Zhaohui Zheng and Yong Chang.

Last, but not the least, I am deeply ingratiated to my family for their understanding and patience, unflinching support and continued unconditional love throughout my whole life.

Contents

Partii Impact of Dispersion on Hybrid of Frequency-Hopped Optical CDMA and WDMA Networks

List of Figures

List of Tables

CHAPTER 1

INTRODUCTION OF PART I——

COMPARISON OF TAVELING WAVE AND GAIN-CLAMPED SEMICONDUCTOR OPTICAL AMPLIFIERS

1.1 Background Information

1.1.1 The History Review of Optical Amplifications

The invention of semiconductor lasers in 1962 indicated the beginning of practical fiber optical communication systems. Today, most of bit flows in long haul system propagate in optical fibers. Two merits decide the silica fibers will replace the copper cables and dominate in information transportation. One is only fibers can provide the huge bandwidth up to Tera-bit per second. The other is fibers are made of silica, which is the most abundant material in nature. So fibers are potentially low cost. Besides the long haul transmission, optical communication is also expanding its applications to some other fields which are never touched before. For example, the optical links between printed circuit boards (PCB) and even between high speed electronic integrated circuits (elC) [1], optical logic[32, 33]. The commercialization of this application will inevitably boom a new market in optical communications, even if it would not start a revolution in signal processing technology.

In the first-generation optical networks, optical fiber is purely a replacement for copper cable. All the controlling and processing of the bit-flow is handled in electronic domain. After tens of kilometers propagation in fibers, the optical signal is greatly degraded so that it has to be regenerated, i.e., the light signal has to be converted to

electronic pulses and then converted to light pulses again. Obviously this conversion makes the system not only high cost but also very complex.

It is natural for people to seek a new way to directly amplifying the signal in optical domain. Roughly from 1963, right after the semiconductor laser was invented, the research on modifying a semiconductor laser to a semiconductor optical amplifier was started. Due to some technology difficulties, such like operation temperature, couple efficiency, optical noise, etc., the operation of devices was still premature.

An important thing happened in 1994. Erbium-doped fiber amplifier (EDFA) was invented, which is a breakthrough in direct optical amplification research and found its commercial application instantly. But EDFAs can only work at the wavelength around 1.55/лп, while the operation wavelength of SOAs covers the whole range of fiber-optic transmission, from 0.8 to 1.55//m. Besides, SOAs are not limited in linear applications, it can be expanded to nonlinear functions, such as wavelength conversion, switching, optical logic, dispersion compensation and tunable wavelength filter, which are key techniques in all-optical networks. What's more, the size of a SOA is so compact that they can be fabricated with other components in a single package to obtain an optical integrated circuit (OIC), and get even better performance with the lower cost. All these exclusive benefits attract people never give up the researches on SOAs [2]. Actually, in the past decade, researches on SOAs achieved rapid progress.

1.1.2 Why Do Simulation

With the increasing of data rates, especially the use of wavelength-division multiplexing (WDM) technique, optical communications gradually achieved more and more features, such as optical switching, data regeneration, and wavelength routing, which make today's optical networks much more complex than the first generation networks. Although photonic systems generally have far fewer components than electronic system, the interactions of the components can be more complicated due to the feedback, reflection,

resonance and intermodulation. As a result, the design of a photonic system can be a truly daunting task.

How can engineers finish such a challenging design and get an optimized design in which so many physical effects are involved? Computer-aided design and engineering (CAD/CAE) is definitely the only choice [3]. CAD/CAE tools for electronic devices and systems design have pushed the electronic devices and systems manufacture to a very mature stage. The research and development of CAD/CAE software also becomes an independent industry and has commercially achieved a howling success. This is a vivid demo to the future development of photonic industry.

The core part of CAD/CAE software is physical model and its numerical algorithm. In photonic devices, photonic and electronic physical effects have to be considered simultaneously, particularly in the case of active devices such as lasers, amplifiers, detectors, etc. That is the reason why the simulation of photonic devices is usually more challenging than that of purely electronic subsystem. This complexity also indicates the necessity to simulate and optimize the design before the fabrications.

1.1.3 The Dynamic Model of Semiconductor Optical Amplifiers

A huge number of papers about semiconductor lasers simulations have been published and commercial CAD/CAE tools are also available. Based on the knowledge of laser simulation, more and more researches are focused on SOAs, because it seems SOAs are the most potential candidate for advanced smart optical network applications, which can provide more control functions rather than the mere transmission.

The difference between lasers and SOAs is that lasers can be treated at a single wavelength while SOAs have to be considered over a wide wavelength band. This is why the SOA modeling is tougher. Some valuable attempts have been done [4-10]. Generally,

there are two types of models, one in frequency domain and the other in time domain. The frequency-domain model may show a detailed property of the lasing spectrum, which is basically a static description. In many simulation applications, for example, to simulate a SOA in a system link, the dynamic time domain model maybe more useful because which can show the detail of each digital bit.

1.2 Scope of The Thesis

This thesis is organized into seven chapters. In Chapter 2, the basic principle of optical amplifiers and their applications, including linear and nonlinear, are introduced. In Chapter 3, after examining the working theory and structure of traveling wave SOAs and gain-clamped SOAs, a time-domain model is developed which covers a wide bandwidth and can be used to simulate both TW-SOAs and GC-SOAs. In Chapter 4, a numerical method to solve the model and the implementation procedure in a TW-SOA and DBR-SOA are described. The equations to obtain the time-domain output power spectrum and noise figure are also given. In Chapter 5, the simulation results of a TW-SOA and a DBR-SOA are presented to validate the numerical solver and compare the two types of SOAs, which are with identical device parameters. Three non-physical simulation parameters are verified to make the solver reliable. In Chapter 6, the dependence on working conditions and device structure are simulated and compared. In Chapter 7, the linear and nonlinear application examples are simulated, including amplification in WDM system and wavelength conversion. Finally, Chapter 8 discusses the overall conclusions and suggestions of future work.

CHAPTER 2

OPTICAL AMPLIFIERS AND THEIR APPLICATIONS

Optical amplifier, as the name implies, is a device that can amplify an input optical signal. Basically there are two types of optical amplifiers, semiconductor optical amplifiers (SOAs) and fiber amplifiers, which operate by different principles and with different configurations.

2.1 Semiconductor Optical Amplifiers

Semiconductor optical amplifiers are also named as semiconductor laser amplifiers, because the operation principle originates from that of semiconductor lasers. Working as an optical source oscillator, a laser has two fundamental mechanisms, amplification and feedback, as same as the situation in an electronic oscillator.

A SOA can be obtained by removing the feedback of a laser. As shown in figure 2.1, the diode consists one or more sandwiched layers of semiconductor doped with impurities, which have different electrical properties. When an electric field is applied to the active region, valence electrons in the crystal lattice leave their places and move through the material leaving behind *holes* in their places that other electrons can fill in. When an electron in conduction band and a hole in valence band recombine in the active region bordered by junctions of the semiconductor material, a photon may be spontaneously emitted, as illustrated in figure 2.2(a). The spontaneous emitted photon is with random

direction and phase, and its wavelength is determined by the material's energy band-gap between the electron-hole pair. The band-gaps of different electron-hole pairs are not quite same therefore the spontaneous emitted photons cover a wide range of wavelength. The radiative recombination may also be stimulated by an existing photon, as shown in figure 2.2(b). The remarkable feature of the stimulated emission is that the emitted photon matches the original photon in both wavelength and the direction of propagation.

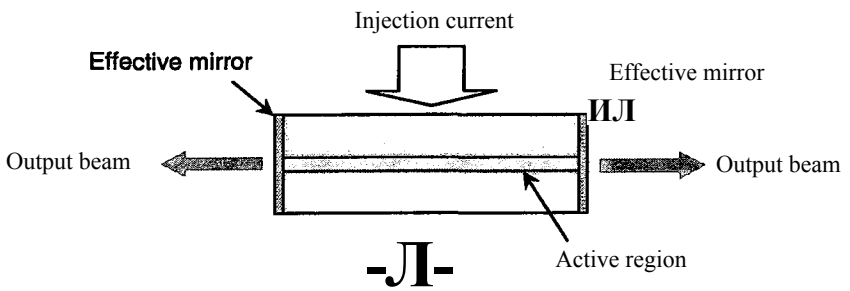

(a) Semiconductor laser

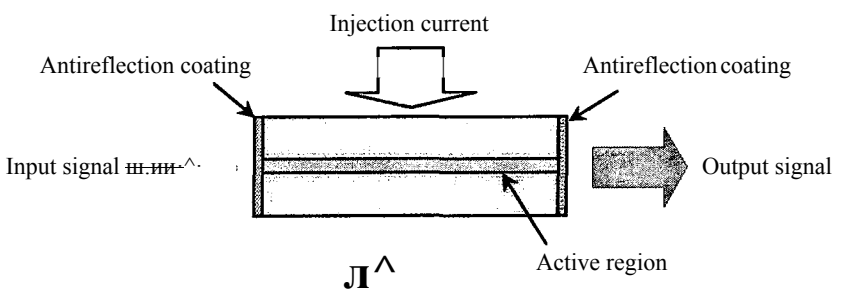

(b) Semiconductor optical amplifier

Fig. 2.1 Schematic diagram of semiconductor laser and SOA

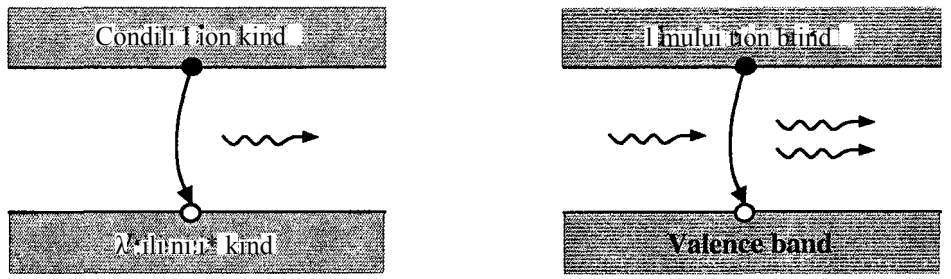

(a) Spontaneous emission (b) Stimulated emission

Fig. 2.2 Schematic illustration of photon emission in semiconductor

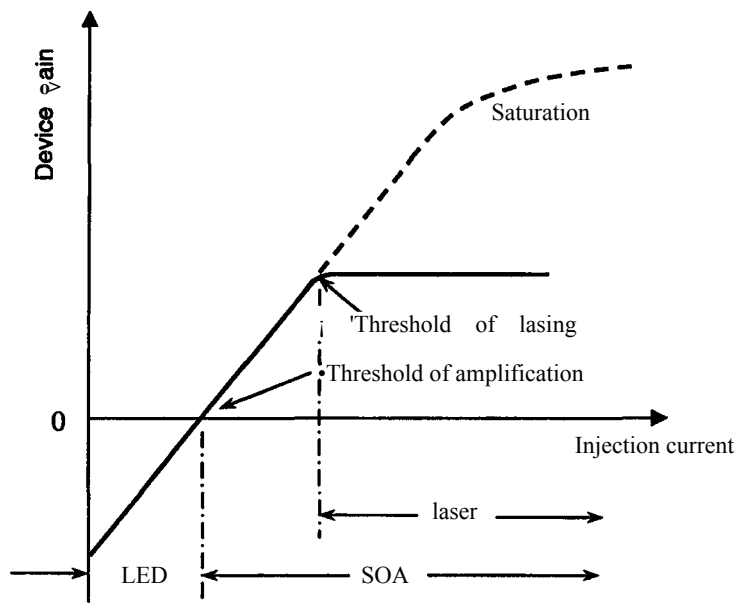

Fig. 2.3 Different operation states of a laser diode

Theoretically a device with a semiconductor laser structure may work at one of the three states, a light-emitting diode (LED), a SOA, or a laser, depending on the magnitude of the injection current, as shown in figure 2.3. When the injection current is relative low, the device just glows due to the spontaneous emission, functioning as an LED. At this point

any light coupled in the device from an external source will be absorbed. With the increasing of the injection electronic current, the internal gain (material gain minors internal lose) will be larger than zero. Above this point the optical amplification begins. As the current is increased further, if the diode has a feedback mechanism such as partially reflective end facets, the gain exceeds all kinds of losses and lasing beam comes out. The diode is a laser. If the feedback is greatly reduced by antireflection coating or any other equivalent technology, the lasing will not occur and the device gain can be pushed higher until moved into the saturation region where the gain will not linearly increased with the pump current, as the dash line indicated in figure 2.3. In this case the device is a typical SOA.

2.2 Fiber Amplifiers

Optical amplification in a fiber by the interaction of a pump with a signal can be classified into two types, Raman amplifiers and area-earth-doped fiber amplifiers. Both types utilize the external laser pump as the energy source to amplify the input signal.

Raman amplifiers take advantage of nonlinear optical phenomena such as Raman and Brillouin scattering, which are initiated by lattice vibrations of the molecules constituting the material of the fiber. In elastic scattering, the incident photon is converted into a lower energy photon while the energy difference is accounted for the emission of an optical (Raman) or acoustic (Brillouin) phonon. The frequency difference between pump (v_p) and signal (v_s) is termed Stokes shift. By simultaneously coupling a pump beam at λ_ρ and a signal beam at $\tilde{A}_s$ into an optical fiber, amplification at Ą is obtained by stimulated Raman scattering or stimulated Brillouiri scattering [11-13]. The shortcoming of nonlinear methods is generally less efficient in transferring energy from pump to signal, and the system configuration is more complex compared with area-earth-doped fiber amplifiers.

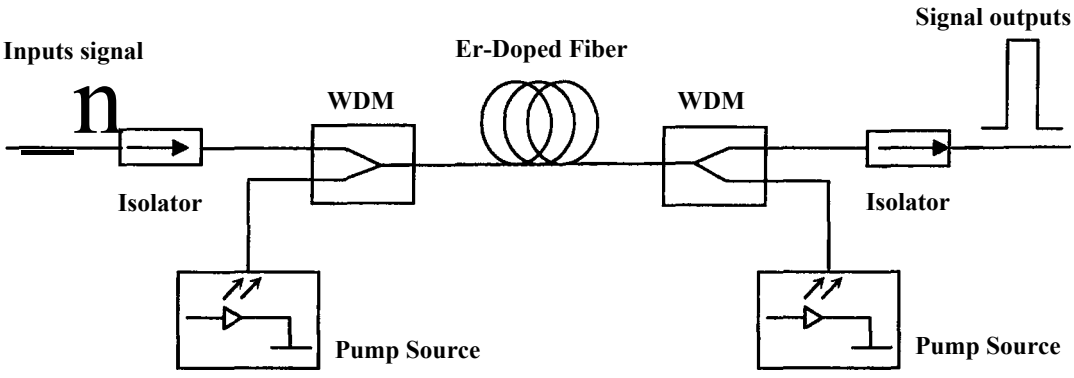

Fig. 2.4 Configuration of EDFA [19]

Fundamental to all area-earth-doped fiber amplifiers is the population inversion of ions from the ground state to an excited state. The pump power injected form external lasers is stored in the excited state from which incoming signals may stimulate emission. The pumping schemes are categorized as either 3- or 4-level systems depending on different dopants, such as Er^{3+} (erbium), Nd^{3+} (neodymium) or Pr^{3+} (praseodymium). The erbium-doped fiber amplifier (EDFA) produces gain in the 1550 nm band , whereas the amplification in the 1310 gain region is provided by neodymium or praseodymium.

As an example, figure 2.4 illustrates the configuration of EDFA. The basic components of an EDFA include a segment of Erbium doped fiber (10 ~ 20 meters), a pump laser, and a wavelength division multiplexer (WDM). When the signal-carrying laser beams pass through this fiber, an external optical pump is applied. These two beams are combined by the WDM multiplexer. Due to the energy band property of erbium [14, 15], the external pump source can be either 980nm or 1480nm, and the signal wavelength is confined in the range between 1530nm and 1620nm. In the segment of Er-doped fiber, the photons of the pump source excite erbium atoms to a higher energy level. The excited erbium atoms are stimulated by the signal photons and emit photons at the same wavelength and direction as the incoming signal. Thus the power of input signals is amplified without change of their original modulation characteristics.

In some applications it is necessary to reject any unused pump light, so an optical filter may be used at both ends of the amplifier. This can be achieved by using a second dichroic coupler, in which case a second laser can be used to pump the fiber from the other end. This will allow the fiber length to be increased; implying increases gain from the amplifier. The isolators at both ends will prevent the spontaneous emission noise traveling backward to the light source.

2.3 The Applications of Semiconductor Optical Amplifiers

So much research has been launched into SOAs because SOA is the most potential active device in both linear and nonlinear applications, and its compact structure makes it very ideal for optical integration. For linear applications SOAs may work as power boosters, in-line amplifiers and preamplifiers.

1. Power Booster

In optical networks, for instance the WDM network, after multiplexing or some other optical processes, the signal power is not necessarily high enough for fiber transmission, particularly in long haul systems. SOAs can boost the signal power to a high level for transmission. The most important parameter for power booster is the output saturation power. Multiquantum-well (MQW) active regions are good solution with very large saturation output powers. And, by introducing stress in the active region of a MQW SOA, the TE and TM gain characteristics can be modified to give polarization independent gain over some wavelength range.

2. In-line Amplifier

The optical power drops exponentially with distance due to the transmission attenuation in fibers. SOAs may work as in-line amplifiers in long haul systems to compensate the attenuation. Some interesting questions for in-line amplifiers are — what is the upper limit on the number of amplifiers that can be cascaded before noise buildup in the

chain causes unacceptable system degradation? What is the optimum amplifier spacing in a long haul system?

3. Preamplifier

In this application a SOA amplifies the optical signal before it falls on the receiver. Preamplifiers are necessary especially in high data-rate system, because the thermal noise in the receiver rises faster than the square of the bit rate. The SOA boosts the signal to such a high level that the receiver performance is limited by shot noise rather than by thermal noise. Therefore the most important parameters for a SOA in such application are the low noise figure and the high input coupling efficiency.

In contrast to linear applications, SOAs nonlinear applications are more significant. Basically the nonlinearities result from the carrier density dependence of the gain and refractive index in the active region of SOAs.

1. Wavelength Converter

All-optical conversion is one of the key technologies in WDM networks [19, 20, 25]. Wavelength converters can reconfigure the network to provide more flexible and novel network management schemes thus allowing for evolution of the network. For example, the node congestion or link failure can be solved by rerouting the optical path to an available wavelength. Wavelength conversion can be achieved by SOAs with the scheme of cross gain modulation (XGM), cross phase modulation (XPM) or four-wave mixing (FWM) [26-28].

2. Tunable Wavelength filter

In a WDM network a bunch of wavelength channels are simultaneously transmitted through a single fiber. The wavelength filter is desired to isolate each channel at the receiving or routing node. The filter resolution is a crucial parameter to minimize the channel spacing and therefore to maximize the number of channel. The tunability of the

filter allows for dynamic network reconfiguration and increases versatility of the system. The wavelength selectivity of these devices is based on the finite time response of the nonlinear optical medium. The filter pass-band is given by the spectral selectivity of the FWM process due to the finite time response of the medium [29]. The filter pass-band is centered on the wavelength of the reference pump source and is therefore widely tunable.

3. Switching

All-optical switch is a key component in future optical networks such as optical time division-multiplexed systems. The optical signal at one channel can be switched to another channel under the control of an optical pulse. This pulse leads to gain saturation due to carrier depletion in SOAs and controls refractive index changes in the gain medium of SOAs. Some switching schemes based on SOAs have been demonstrated [30, 31].

4. Optical Logic

All-optical logic is a challenging and exciting topic because it is the fundamental element of optical computers. Digital logic is basically nonlinear. The nonlinearities of SOAs, such as XGM, XPM and FWM, determine SOA is the most potential candidate to play a roll which in electronic computer is played by electronic transistor. SOA-based all-optical NOT, NOR and XOR have been successfully demonstrated [32-34].

SOAs are prospective devices for future optical networks due to their compact size, single component, ultra-wideband gain spectrum, low power consumption, low cost, and integration with other device. In contrast to fiber amplifiers, which have been widely deployed in practical systems, SOAs are more potential for future development for both linear and nonlinear applications.

CHAPTER 3
TIME-DOMAIN DYNAMIC MODEL OF GC-SOAs

By analyzing the structure of gain-clamped SOA, a time-domain dynamic model is developed in this chapter. This model can be applied to both TW-SOAs and GC-SOAs. Its key elements consist of traveling-wave equation, boundary condition, carrier rate equation and material gain.

3.1 Gain-Clamped Semiconductor Optical Amplifiers

Gain dynamics plays a key role to determine the characteristics of SOAs [16]. Since the gain of a SOA comes from the stimulated emission in the recombination process of injection electronic carriers, if there are two or more input channels each with a unique wavelength, the recombinations stimulated by different channels will compete for carrier consuming so that each channel will be modulated by the signals of other channels. This phenomenon is called cross-gain modulation (XGM) [17, 18]. XGM in conventional SOAs can be applied to all-optical wavelength conversion [19, 20], but it can also lead to serious channel-to-channel crosstalk in WDM networks.

In order to overcome the crosstalk problem, gain-clamped SOA is proposed [21, 22]. As shown in figure 2.3, after a laser begins to lasing, the gain is independent of the inject current. The increase of injection current just leads to the rising of output optical power,

and vice versa. That indicates, for certain injection current of the lasing laser, if the input optical power varies, the lasing output will function as a valve to automatically retain the carrier density at a constant, so that a constant gain is obtained.

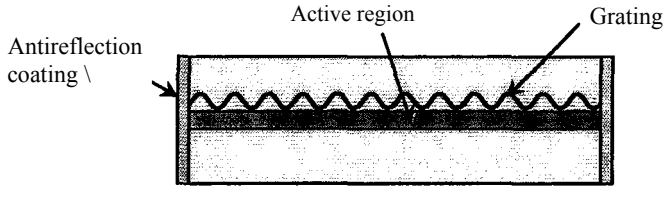

(a) DFB structure GC-SOA

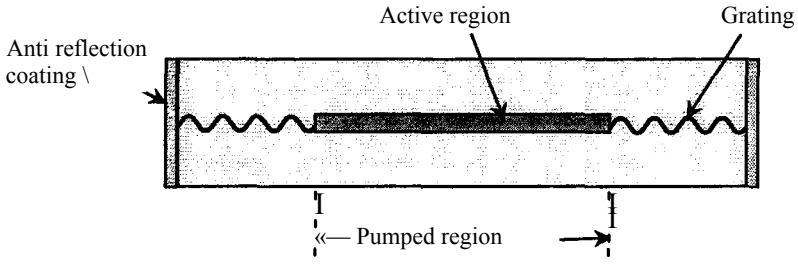

(b) DBR structure GC-SOA

Fig. 3.1 Schematic configuration of GC-SOAs

This idea can be achieved by either distributed feedback (DFB) or distributed reflector (DBR) structures [23], as shown in figure 3.1. With antireflection coatings DFB or DBR lasers can be modified to obtain SOAs. In DFB lasers, the grating is etched onto one of the cladding layers rather than the active layer, because direct etching of the active layer will increase the rate of nonradiative recombination. The lasing wavelength is at one of the pass bands which are right beside the stop band of the grating [4]. In contrast to a DFB laser, a DBR lasers is effectively an FP laser but whose mirror reflectivities are wavelength-dependent. Lasing occurs at the wavelength with maximum reflectivity, i.e., the Bragg wavelength [24]. By an appropriate design of the feedback structure, mainly

the grating period, the device can lase at a wavelength that is away from the wavelength of amplified signals.

The lasing spectra of DFB and DBR lasers are different, but their contribution to gain dynamics is quite similar. Thus their performances are similar. In this thesis the GC-SOAs with DBR structures are simulated to compare the performances of GC-SOA and TW-SOA. The device structure is illustrated in figure 3.1(b).

3.2 Time-Dependent Traveling-Wave Equations

In a single mode laser, most injection carriers are depleted at the single mode, so that only the wave equation at the lasing mode is employed to conduct the simulation. However, in a SOA, carriers are depleted in a broad bandwidth (hundreds of nanometers) no matter whether there is a signal propagating in the cavity or not. That means the wave equations of a SOA must cover a lot of modes rather than only a single mode.

Because the reflectivities of facets can't be reduced to zero by AR coating, the spontaneously emitted noise will show the presence of longitudinal cavity modes. We assume that noise fields *concentrate* at discrete frequencies corresponding to cavity modes. The frequencies can be approximated by

$$v' = m\frac{c}{4L} \qquad (3.1)$$

where L is the length of cavity, n_g the group refractive index and c the vacuum light speed. Therefore the electric field in the SOA cavity can be approximated by

$$E(x, y, z, t) = \sum_{\kappa} (x, y)[F_k(z,t)e^{-J\beta * z} + R_k(z,t)e^{J\beta \wedge '} \qquad (3.2)$$

where $\psi_k(x,y)$ is the fc-th transverse fields which is assumed to be independent on longitudinal fields. This assumption is valid for SOAs with narrow active regions that is true in most lasers and SOAs. $F_k(z,t)$ and $R_k(z,t)$ are the fc-th slowly varying field amplitudes of the forward and reverse waves, respectively. to_k (= $2nv_k$) is the *k-th* reference angular frequency.

From Maxwell's equations, we can write the time-dependent wave equation in a waveguide with uniform grating as [chapter 7 of ref. 24]

$$\begin{aligned} &\frac{1}{v_{g,k}}\frac{dF_k(z,t)}{dt} + \frac{dF_k(z,t)}{dz} = \left(\frac{G_k - \alpha_{in}}{2}\right)F_k(z,t) + j\kappa R_k(z,t)\exp(-j2\Delta\beta z) + s_k^F(z,t) \\ &-\frac{1}{v_{g,k}}\frac{dR_k(z,t)}{dt} - \frac{dR_k(z,t)}{dz} = \left(\frac{G_k - \alpha_{in}}{2}\right)R_k(z,t) + j\kappa^* F_k(z,t)\exp(-j2\Delta\beta z) + s_k^R(z,t) \end{aligned} \tag{3.3}$$

$$G_k = \frac{1}{2}(g_m - \alpha_{in}) \qquad \Delta\beta = \beta_k - \frac{\pi}{\Lambda} \qquad \beta_k = \frac{2\pi n_{eff,k}}{\lambda}$$

The parameters used are defined by

$v_{g,k}$ — Group velocity at the *κ-th* mode;

κ — Coupling coefficient;

S_k —Detuning factor;

β_k — Porpagation constant;

$n_{eff,k}$ — Effective-mode index;

g_m — Material gain;

a_{in} — Internal material loss;

Γ — Optical confinement factor;

s_k^F, s_k^R — Locally generated spontaneous emission noise, forward and backward.

In general, the effective refraction index is related to both carrier density and frequency. This physics must be covered in wideband devices such as a SOA. For simplicity the effective refractive index can be linearly approximated by

$$n_{eff}(\nu_k, N) = n_{eff0} + \frac{dn_{eff}}{d\nu}(\nu_k - \nu_0) + \frac{dn_{eff}}{dN}(N - N_0) \,. \tag{3.4}$$

The material loss coefficient a_{in} (m̄ 1) is also linearly approximated by [8]

$$a_{in}(N) = K_0 + TK_l N \tag{3.5}$$

where N is the carrier density, K_0 represents the intrinsic material loss, and K_l depends mainly on intervalence band absorption.

Petermann [39] proved that the spontaneous emission fields coupled to forward and reverse waves have equal amplitudes, e.g., $s(z,t) = s£(z,t) = {}_{k}s^{*}(z,t)$. The spontaneous emission noise is generated from a Gaussian distributed random number generator that satisfies the correlation [10,40,41]

$$\left\langle s_k(z,t)s_k^*(z,t)\right\rangle = \gamma\frac{R_{sp}}{L}\delta(z-z')\delta(t-t') \tag{3.6}$$

where R_{sp} is the spontaneous emission rate per unit length of the cavity (s'rri[1]), which is given in the material gain model, γ is the coupling factor accounting for the spontaneous emission coupled into the forward and reverse waves. L is the length of active region.

3.3 Boundary Condition

Eq.(3.3) is used to cover both signal and noise fields at all wavelengths. The boundary condition can be expressed by a general equation

$$\begin{aligned} F_k(0) &= (1-r_1)F_{in}+r_1 R_k(0) \\ R_k(L) &= (1-r_2)R_{in}+r_2 F_k(L) \end{aligned} \tag{3.6}$$

where and F_{ink}, R_{iuk} are the κ-th forward and reverse input signals, respectively. F^ and R_{ink} are zeros at the wavelengths without input signal. r_x, r_2 are the facet amplitude reflectivity coefficients.

The forward and reverse input signal powers P-^$_k$ and P^ and the fields inside the facets satisfy

$$F_{ink} = \sqrt{\frac{\eta_1 P_{ink}^F}{h\nu_k}}, \quad R_{ink} = \sqrt{\frac{\eta_2 P_{ink}^R}{h\nu_k}} \tag{3.7}$$

where η_λ and η_2 are coupling efficiencies at the two facets. The output powers

$$P_{outk}^F = h\nu_k \eta_2 \left|(1-r_2)F_k(L)\right|^2, \quad P_{outk}^R = h\nu_k \eta_1 \left|(1-r_1)R_k(0)\right|^2. \tag{3.8}$$

According to Eq.(3.7) the relationship between field amplitudes $F_k(z,t)$ and $R_k(z,t)$ and the photon rates S_f and S_k (s^{-1}) satisfies

$$\left|F_k\right|^2 = S_k^F, \quad \left|R_k\right|^2 = S_k^R. \tag{3.9}$$

3.4 Carrier Rate Equation

The carrier rate equation is a continuity equation to describe the dynamics of injection carrier density (m^{-3}) and generated photon rate (s^{-1}). The injection carriers are depleted by various recombinations, which is governed by

$$\frac{dN(z)}{dt} = \frac{I}{edLW} - R_{rec}(N(z)) - \frac{\Gamma}{dW}\left\{\sum_k g(\nu_k, N(z))\right|F_k \quad \omega + \kappa * (\zeta\{\} \qquad <3Л0)$$

where I — amplifier bias current;

e — elementary charge;

d, W, L— depth, width and length of the active region.

The first term on the right hand side (RHS) of Eq.(3.10) represents the rate of injection carrier density (m"3s-1). Here we assume that all the bias current passes through the active region only(rather than the surrounding InP regions), and the current has a uniformdistribution across the active region. The injection carriers are depleted by various mechanisms. These mechanisms are categorized into two groups, amplification non-related and amplification related, which are accounted by the second and the third terms on the RHS of Eq.(3.10), respectively.

The second term $R_{rec}(N)$ consists of both the radiative recombination rate $R_{rad}(N)$ and nonradiati ve recombination rate $R_{nrad}(N)$.

$$Rr_e cW) = R_{rad}(N) + R_{nrBd}(N) \qquad (3.11)$$

$R_{rad}(N)$ and $R_{nrad}(N)$ can be approximated by polynomial functions of carrier density N [35, 36]

$$Rraä(N) = A_{rad}N + B_{raä}N^2$$
$$Kraä\ (N) = A_{nrad}N + B_{\eta\Gamma\alpha 4}\ N^2 + C_{aug}N^3 \qquad (3.12)$$

A_{rad} and B_{rad} are the linear and bimolecular radiative recombination coefficients. A_{nrad} is a linear nonradiative recombination coefficient due to traps in the semiconductor material. B_{nrad} accounts for nonradiative bimolecular recombination. C is the Auger recombination coefficient. As shown in Eq.(3.12) the Auger recombination will play a key roll with high carrier density. It should be noted that here we neglect the carrier leakage from the active region into surrounding InP region.

The last term on the RHS of Eq.(3.10) represents the carrier depletion due to the amplified signal and amplified spontaneous emission (ASE) noise. Only the photons in active region play rolls in the radiative recombination of carriers. So the optical confinement factor Γ is included. In this model, the SOA is assumed to be polarization independent. Otherwise, two different optical confinement factors should be applied to TE and TM modes.

3.5 Material Gain and Spontaneous Emission Noise

The optical signal can be amplified by a SOA is physically due to the material gain of the device. A lot of research has been done for the optical gain of semiconductor material. This thesis aims at the SOA model rather than devices. We only consider a bulk InP-InGaAsP as an example to exam the feasibility of the model. Hereby we use the following gain model [8] which is relatively simple and good enough for our purpose.

The bandgap energy E_g is written by

$$E_g(N) = E_{g0} - AE_g(N). \tag{3.13}$$

E_{g0} is the bandgap energy when there is not injection current, which can be expressed by quadratic approximation

$$E_{g0} = e(a + by + cy^2) \tag{3.14}$$

where e is the electronic charge, a, b, c the quadratic coefficients. AE_g is the bandgap shrinkage which is due to the injected carriers and leads to the shift of the peak of the gain and spontaneous emission spectra toward shorter wavelengths.

$$AE_g(N) = eK_g N'^{/3} \tag{3.15}$$

K_g is the bandgap shrinkage coefficient.

The quasi-Fermi level of the conduction band E_{fc} is relative to the bottom of the band, and the quasi-Fermi level of the valence band E_p is relative to the top of the band. They can be written with Nilsson approximation as [37]

$$E_{fc} = KT\left\{I\eta\delta + \delta\left[64 + 0.05524\mathrm{J}\,(64 + \sqrt{\delta})\right]^{-1/4}\right\}$$
$$E_p = -kT\left\{\eta\varepsilon + \varepsilon\left[64 + 0.05524\mathrm{f}(64 + J\ddot{e})\right]^{1/4}\right\} \tag{3.16}$$

where

$$\delta = \frac{N}{N_c}; \qquad \varepsilon = \frac{N}{N_v}. \tag{3.17}$$

N is the carrier density. N_c and N_v are constants given by

$$N_c = 2\left(\frac{m_e kT}{2u_t^e}\right)^{3/2}; \qquad N_v = 2\left(\frac{^m di, kT}{2\pi\eta^2}\right)^{3/2} \tag{3.18}$$

where

$$m_{dh} = \left(m_{hh}^{\frac{3}{2}} + Щu^{\frac{3}{2}}\right)^{\frac{2}{3}}. \tag{3.19}$$

m_{lh} and m_{hh} are the effective mass of the light hole and heavy hole in the valence band, respectively. T is absolute temperature and κ the Boltzmann constant, η is Planck's constant h devied by $2\ \pi$.

The Fermi-Dirac distributions in the conduction band and valence band are given by [38]

$$\begin{aligned} /» &= \left[1 + \exp\left(\frac{E_a - E_{fc}}{kT}\right)\right]^{-1} \\ ЛИ &= \left[1 + \exp\left(\frac{(E_b - E_{fc}}{kT}\right)\right]^{-1} \end{aligned} \tag{3.20}$$

where

$$\begin{aligned} E_a &= (h\nu - E_g(N)\} \quad \frac{m_{hh}}{m_e + m_{lh}} \\ E_b &= -(h\nu - E_g(N)\} \quad \frac{m_{v,}}{m_e + m_{hh}} \end{aligned}. \tag{3.21}$$

From the above, the material gain coefficient g_m (m '1) of the InGaAsP bulk-material can be derived by [8]

$$g_m W) = - \quad \frac{S}{\tau}\left(\frac{f_c^{\backslash}}{Jm_l v_j}\right)^2 \left(\frac{\text{и}\ll''\text{Ц}}{\text{Ш}_e + m_{nn}}\right)^{3/2} \sqrt{h\nu - E_g(N)}\left(f_c(\nu) - f_v(\nu)\right) \tag{3.22}$$

where c is the speed of light in vacuum, n_t the refractive index at active region, m_e the effective mass of electron in the conduction band, τ is the radiative carrier recombination lifetime approximated by

$$\tau^{-1} = A_{rad} + B_{rad} N \tag{3.23}$$

where A_{rad} and B_{rad} are the linear and bimolecular radiative recombination coefficients.

The material gain g_m consists of two components, g'_m and g''_m.

$$\bar{8}_m = \bar{8}_m + \bar{8}_m \tag{3.24}$$

where

$$g'.(V.N) = \frac{\sqrt{2}}{\tau}\left(\frac{/>}{\text{K}hn_x v}\right)^{I}\left(\frac{m_e m_{hh}}{m_e + m_{hh}}\right)^{3/2} J\overline{h\nu - E_g(N) f_c}\ (\text{i/})(1 - f_v\ (\nu)) \tag{3.25}$$

$$8''.W) = \frac{\sqrt{2}}{T}\left(\frac{r}{hn_1\nu}\right)\left(\frac{m_e m_{hh}}{m_e + m_{hh}}\right)^{3/2} J\overline{h\nu - E_g(N)}(1 - f_c\ (y))f_v\ (y) \tag{3.26}$$

The spontaneous emission photons coupled into a waveguide mode can be calculated by the spontaneous emission rate (s 'm^{-1}) [8]

$$R_{sp}(y,N) = Tg'_m\{v,N)'Av. \tag{3.27}$$

CHAPTER 4
MODEL IMPLEMENTATION

In this chapter, the mathematical model described in Chapter 3 is converted to a numerical format which is easy to be simulated on a computer. The procedure to code the model to a computer program is presented. At last, the method to obtain the time domain output power spectrum and noise figure are also given.

4.1 Numerical Method to Solve Wave Equations

The model described in Chapter 3 covers three domains, time, frequency, and 1-D space. To solve all the equations, a split-step method is applied to the computer implementation. Firstly the 1-D structure is divided into a number of sections along longitudinally directions. If the number of the sections is large enough so that the length of each section is short enough, the wave equation (3.3) can be approximated by [18]

$$\begin{aligned} F_k(z + Az, t + At) &= \exp[(G^* - jS_k)Az]f^*(z,i) + jf(AzR_k(z + \Delta\zeta, i) + {}^{F}s_k\, Az \\ R_k(z, t + At) &= \exp[(G^* - j\delta_k)\Delta\zeta]K^*(z + Az,\ t) + jtc^*AzF_k(z, {}^{R}t) + s_k Az \end{aligned} \qquad (4.1)$$

$$G_k = \frac{1}{2}\left(\Gamma g(n, \nu_k) - \alpha_{in}\right) \qquad \delta_k = \beta_k - \frac{\pi}{\Lambda} \qquad \beta_k = \frac{2\pi\nu_k n_{eff,k}}{c}$$

The physical meaning of Eq.(4.1) is illustrated in figure 4.1. In the forward direction, the first term on the RHS of Eq.(4.1) represents the amplified field which is coupled in from the preceding subsection. The second term represents the reflected filed which comes from the reward direction due to DFB structure and couples into the forward direction field. The last term is spontaneous emission noise. We may numerically assume the noise is inserted into the fields at the virtual boundary of each subsection. The forward noise is added to the forward field at the right virtual boundary, and the reward noise is added to the reward field at the left virtual boundary.

Eq.(4.1) can be applied to two special cases of a GC-SOA, the DBR region (without optical gain) and the active region (without DBR grating), as shown in figure 4.2. In the first case the material gain $g = 0$ and no spontaneous emission noise thereby we have

$$\begin{aligned} F_k(z + Az, t + At) &= \exp\left[\left(-\frac{K_0}{2} - j\delta_k\right)Az\right]F_k(z,t) + jtcAzR_k\{z + Az, t) \\ R_k(z, t + At) &= \exp\left[\left(\frac{K_m}{} \right)Az\right]R_k(z + Az, t) + j\overset{*}{K}AzF_k\{z,t) \end{aligned} \tag{4.2}$$

where K_0 is given in Eq.(3.5).

In the active region of a DBR-SOA and/or the TW-SOA, there is a uniform gain material without the grating structure thereby the coupling coefficient $\kappa - 0$. Eq.(4.1) is in the form of

$$\begin{aligned} F_k(z + Az, t + At) &= \exp[(G^* - j\beta_k)Az]f^*(z,t) + \overset{F}{s}_k Az \\ R_k(z, t + At) &= \exp[(G^* - j\beta_k)Az]R^*(z + Az, t) + \overset{R}{s}_k Az \end{aligned} \tag{4.3}$$

Eqs.(4.2) and (4.3) can be applied to both DBR-SOA and TW-SOA and easily solved by a computer program. The procedure is shown in figure 4.2.

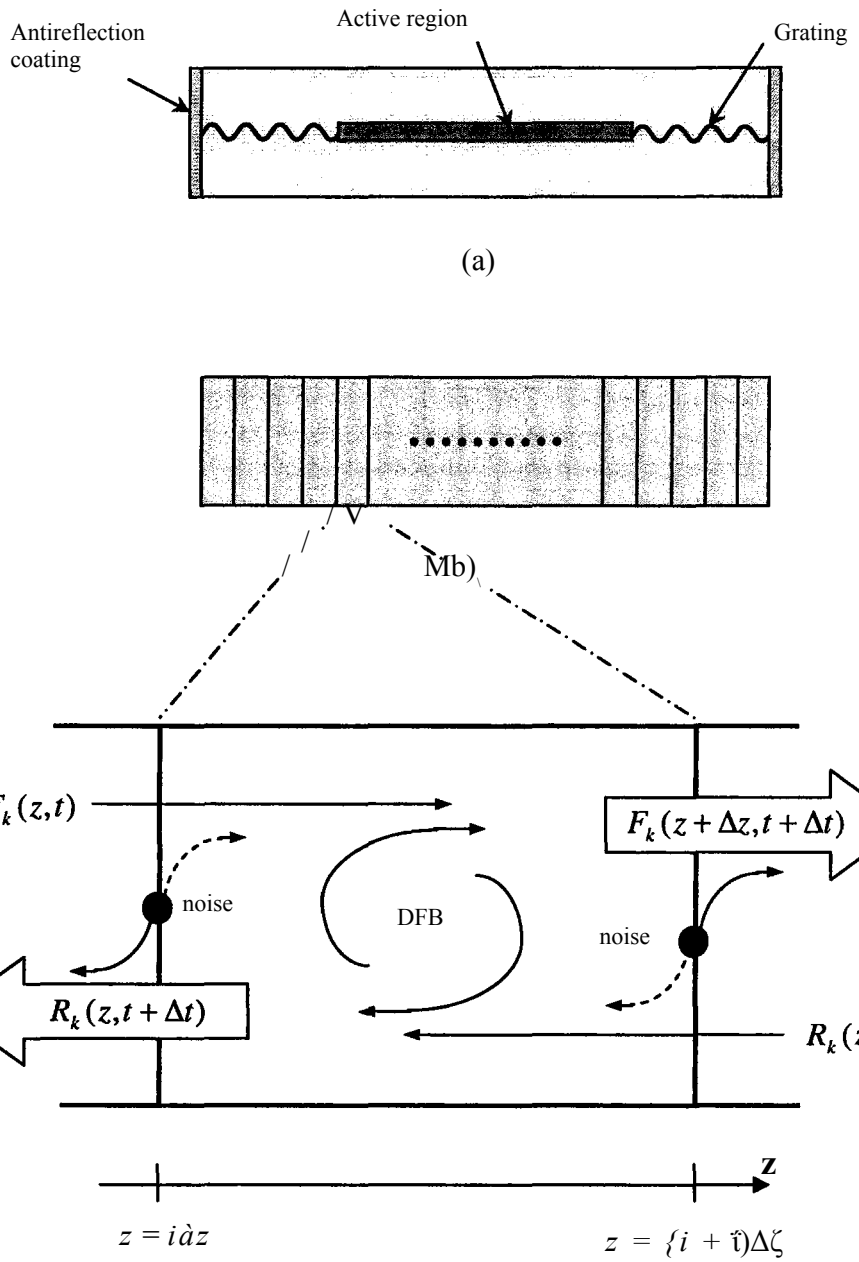

Fig. 4.1 Schematic view of (a) DBB-SOA (b) Virtual sections, and (c) The *Xn* section of numerical model.

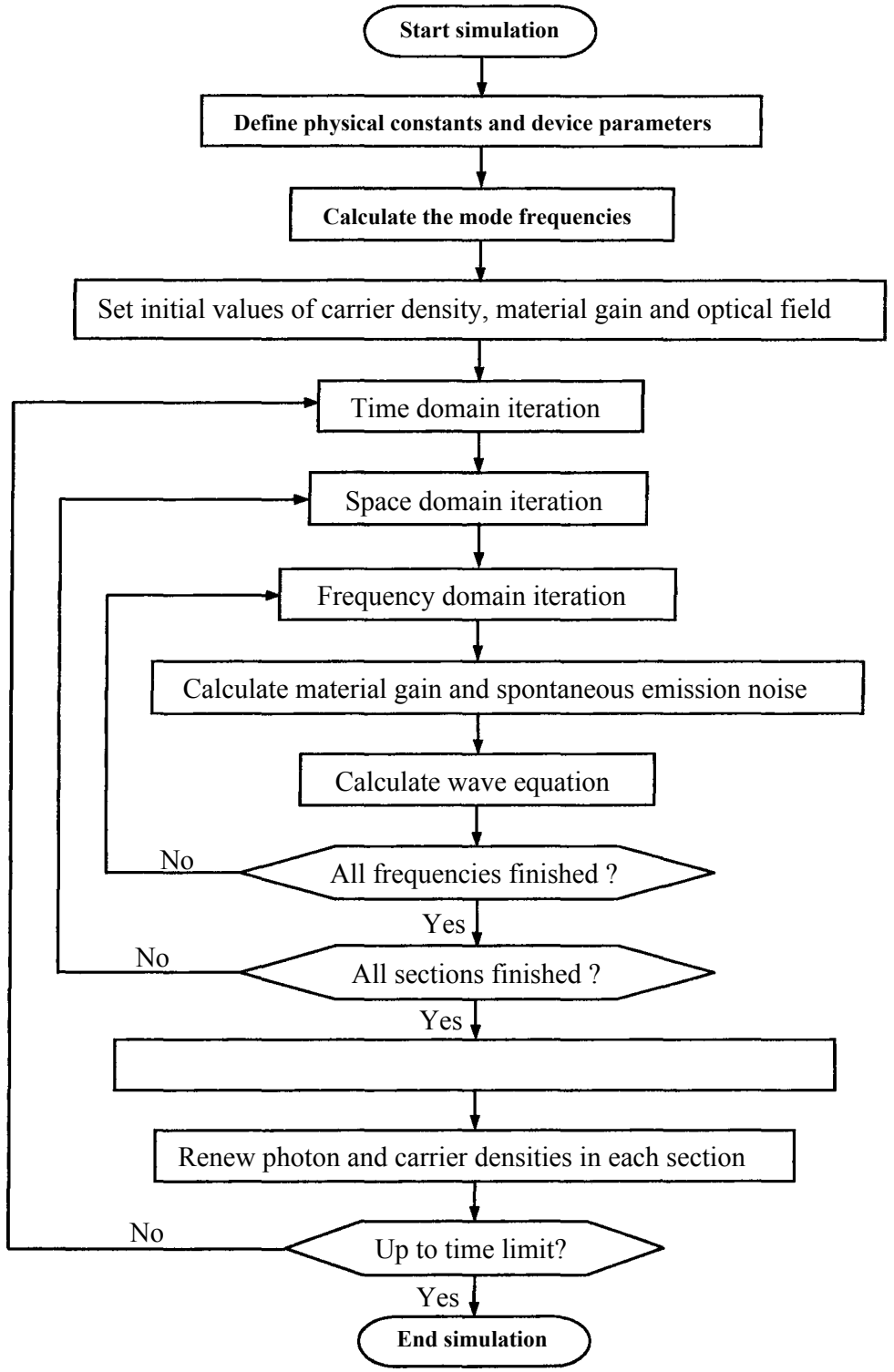

Fig. 4.2 Procedure for the implementation of the SOA model

4.2 Implementation Procedure

The first step of simulation is to define the physical constants and device parameters. This model is in 1-D thereby independent on cross-section profile. In space domain the device parameters and gain are only the functions of longitudinal direction. Therefore this model can be used to simulate the behavior of SOAs with different lateral structures.

The second step is to calculate the mode frequencies. As described above, the physical behavior of a SOA covers a broad band of wavelength. Therefore the mode frequencies need to be obtained, as modeled by Eq.(4.1). With Eq.(3.1) the frequency spacing between two adjacent modes can be approximated by

$$\mathrm{Av} = \frac{c}{2 n_g L} \tag{4.4}$$

Thus the mode frequencies can be expressed by

$$v_k = v_0 + kAv \ (* = 0,1,2A \ , M_k) \tag{4.5}$$

where v_0 is a frequency offset used to match v_k to a resonance and $0 < v_0 < A\ v$. Av is so small that the variation of gain between v_k and $v_k + Av$ is neglectable, thus v_0 is also neglectable. In order to reduce the time cost of simulation, it is not necessary to calculate the wave equation at each cavity mode. It can be simplified by *combining* several modes into one and then calculated at one frequency. Thereby Eq.(4.5) is updated to

$$v_j = v_o + jK_d Av \qquad \begin{pmatrix} \dot{y} = 0,1,2A \ , Mj \\ K_d - Mj = M_k \end{pmatrix}_J \tag{4.6}$$

We name the integer K_d as frequency discretization factor, which denotes how many cavity modes are combined together to be calculated by a single wave equation. Since the majority of optical carrier combinations are contributed to signal amplification and lasing process, this simplification will not introduce too much error, if the frequency discritization factor K_d is not too large. K_d can be determined by numerical experiment which is conducted in chapter 5.

For simplicity and efficiency we confine our simulation in the frequency range with positive material gain. With Eq.(3.22) we chose the minimum frequency as

$$v \wedge > E j h . \tag{4.7}$$

Starting from the minimum frequency the mode frequencies can be calculated with Eqs.(4.4) and (4.5). The simulated wavelength range is about on the order of -100 nm, which is also determined by numerical experiment and conducted in chapter 5.

The third step is setting the initial value. In a real device the carrier density is zero until the electronic current is pumped into the doped region. The analysis of the carrier dynamics require another model which is out of the scope of our purpose. From the application point of view we are more interested in the dynamics when the device is working in a quasi-static situation, i.e., when the device is working to amplify an input optical signal. Therefore we assign a guess value to the initial carrier density, which is near the normal value when a SOA is working, for example, 10^{24} (m^{-1}). By this way the simulation can move into a stable state with the shorter time. The initial values of optical fields $F_k(z,t)$ and $R_k\{z,t)$ are zeros.

The fourth step is to trigger the iteration loops. The time domain iteration starts after all associated parameter calculations are finished. The space domain and frequency

domain iterations are embedded in the time domain loop. The waveguide is sliced into a number of sections along longitudinal direction. In each section the carrier density, gain and effective index are processed as constants in space domain, mean while the gain and effective index are also functions of frequency. In each section, including the active region and the passive DBR region, the wave equations are solved by Eq.(4.1) and (4.3). After frequency domain and time domain calculations are done, the boundary condition Eq.(3.6) is applied to obtain the optical fileds at the two facets. The input optical signal is also coupled into the cavity via the boundary condition implementation. And then, photon and carrier densities are updated for the iteration of next time slot.

Theoretically, the time window of this model can be as long as desired. The time domain optical signal is input from the left facet of the cavity and output from the right one. With Eqs.(3.7) and (3.8) the diagram of power output verse input can be figured out. And many device characteristics can be simulated and thereby optimized.

4.3 Time Domain Output Spectrum

In order to figure out the optical output spectrum in the time domain model, the output signal and noise at the right facet is averaged over time domain. The average output photon rate spectral densities [photon] after counting the coupling loss over both polarizations are

$$\sigma(\nu_*) = \frac{2\eta_{out}(1-R_2)|F_k|^2}{\Delta\nu}. \qquad (4.8,$$

This photon rate spectral densities are centered at ν_k and over the bandwidth $\Delta\nu$. ν_k are defined in Eq.(4.5) and can be deemed as the cavity resonant frequencies. The anti-resonant frequencies are given by

$$v\backslash = V, + \Delta v/2 \qquad (jfc = ОД,2Л\,, M_k) \tag{4.9}$$

The cavity gains at resonant and anti-resonant frequencies are given by

$$\begin{aligned} G_{res}(П) &= \frac{(1-R_1)(1-R_2)G_s(\nu_k)}{(1-ДкГо,(п))} \\ G_{ares}(\nu_k) &= \frac{(1+R_1R_2)G_s(\nu_k)}{(1+ДяТG,W)} \end{aligned} \tag{4.10}$$

where G_s is the single pass gain given by

$$G_s(\nu) = \exp\left[-j\int_z [rg(n,\nu) - a_{in}\right] dz \tag{4.11}$$

With Eq.(4.10) we have the average cavity gains at each mode

$$G_{aver,k} = \frac{G_{res}(\nu_k) + G_{ares}(\nu'_k)}{2} \tag{4.12}$$

The amplifier gain profile is obtained by fitting the cubic spline to the resonant and anti-resonant points. With gain profile the output photon rate spectral densities at resonant and anti-resonant points are given by

$$\begin{aligned} \sigma_{res}(\nu_k) &= \sigma(\nu_k)\frac{G_{res}(\nu_k)}{G_{aver,k}} \\ \sigma_{ares}(\nu'_k) &= \sigma(\nu'_k)\frac{G_{ares}(\nu'_k)}{G_{aver,k}} \end{aligned} \tag{4.13}$$

The discretized output power spectrum is obtained by

$$\begin{aligned} Pou,M &= hv_k - < T_{res}\{v_k)\tilde{} \frac{\Delta v}{1} \\ Po_M(v\backslash) &= hv\backslash - a_a re_S(v\backslash)\tilde{} \frac{\Delta v}{2} \end{aligned} \quad (4.14)$$

It should be noted that the above output power spectrum can only be displayed on an optical spectrum analyzer with a wavelength resolution $\Delta\lambda = \varepsilon\Delta v/v^1$.

4.4 Noise Figure

Noise figure is an important parameter to evaluate the noise degradation of an amplifier. It is defined as the ratio of input signal-noise ratio to output signal-noise ratio.

$$F_n = \frac{SNR_{in}}{SNR_{0Ui}} \quad (4.15)$$

Since the amplifier is sliced to multi-section as if a cascaded sub-amplifier system. Thus the total noise figure of such a system is given by [42]

$$\rho\eta = \rho\eta\alpha)^{+} - \wedge \frac{P\text{-}i(2)}{Gi\ G,G_2} + \blacksquare \frac{\hat{}i(3)}{GjG_2A\ G_{m\_,}} \cdot \quad (4.16)$$

where $F_{n(i)}$ is the noise figure of n-th sub-section which is given by

$$F_{n\,\overline{V)}} \quad \frac{2n_{sp}(i,\tilde{A}_k)\{G_i\text{-}l) + l}{G_i} \quad (4.17)$$

G, is the single pass gain of ith sub-section.

$$G, = \exp\{[rg(i, \Pi_{\kappa}) - a_{in}]\Delta\zeta\} \tag{4.18}$$

n_{sp} is known as the population-inversion factor, expressed by

$$n_{sp}(i, \lambda_k) = \frac{g'(i, \lambda_k)}{g'(i, \lambda_k) - g(I, \Pi_{\kappa}) - a_{bl}} \tag{4.19}$$

where g' and g" are given by Eqs.(3.25) and (3.26).

CHAPTER 5
MODEL VALIDATION

The model described in Chapter 3 and 4 is applied to simulate a DBR-SOA and a TW-SOA. The simulation results are presented to validate the numerical solver and compare the two types of SOAs which are with identical device parameters. Three simulation parameters are verified to make the solver reliable.

5.1 Device Structure and Material Gain

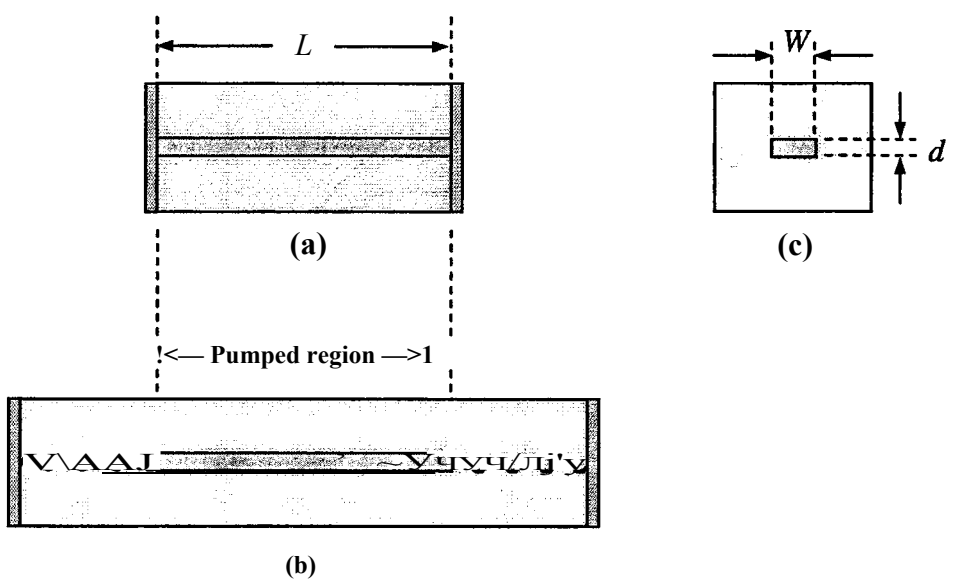

Fig. 5.1 Schematic configuration of (a) longitudinal profile of a TW-SOA,
(b) profile of a DBR-SOA, and (c) the cross-section of the two SOAs.

Both of the simulated SOA's are based on a 1.55 $\mu\tau\eta$ InP-Ini.$_x$Ga$_x$As$_y$Pi.$_y$ homogeneous buried ridge stripe structure with a rectangular cross-section shown in figure 5.1. y and x are the molar fractions of Arsenide and Gallium, respectively, in the undoped active region. Lattice matching is assumed thereby $x = 0.47\ y$. All device structure and material parameters are detailed in appendix. In order to compare the behaviors of the DBR-SOA and TW-SOA, the only difference of our numerical experiment subjects is that DBR-SOA has two distributed grating reflectors. All the material, facets reflectivities, dimensions and other parameters of the two SOA's are identical.

With Eqs.(3.22, 3.25) the typical spectral plot of g_m and g_m ' is given in figure 5.2. To speed up the simulation g_m and g_m' is approximated by a polynomial that is a function of wavelength and carrier density. Because this approximation is valid only for wavelength near the gain peak, the following simulation is confined to a certain scope according to this limit.

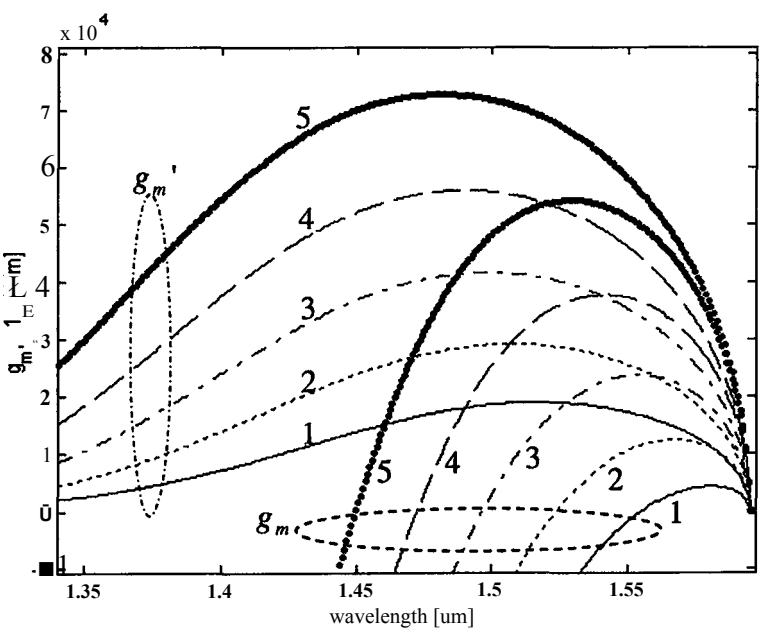

Carrier density: [m'[a]]

(1) l.OxlO^{24}

(2) 1.2X10^{24}

(3) 1.4x1o^{24}

(4) 1.6 XIO^{24}

(5) I.δχIO^{24}

Fig. 5.2 g_m and g_m ' of typical InGaAsP bulk semiconductor

5.2 Model Validation

Before we apply the model to further simulation of SOA devices, the correctness of the model and its numerical algorithm is validated in this section.

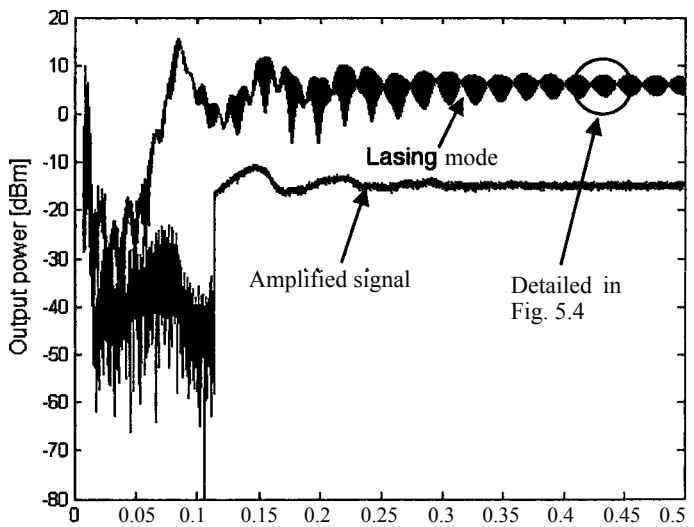

(a) Simulation time of DBR-SOA [ns]

Bias current = 200 mA
Input signal power = -25 dBm
Signal frequency = 1550 nm
Lasing frequency = 1530 nm

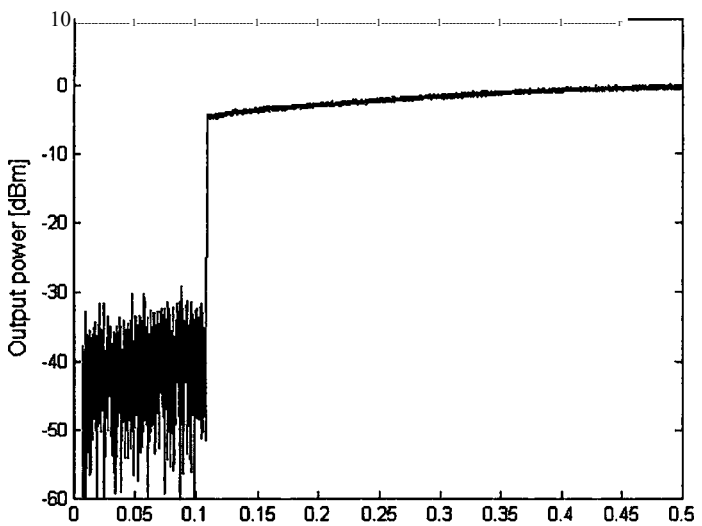

(b) Simulation time of TW-SOA [ns]

Bias current = 90 mA
Input signal power = -25 dBm
Signal frequency = 1550 nm

Fig. 5.3 Time domain output powers of (a) DBR-SOA and (b) TW-SOA

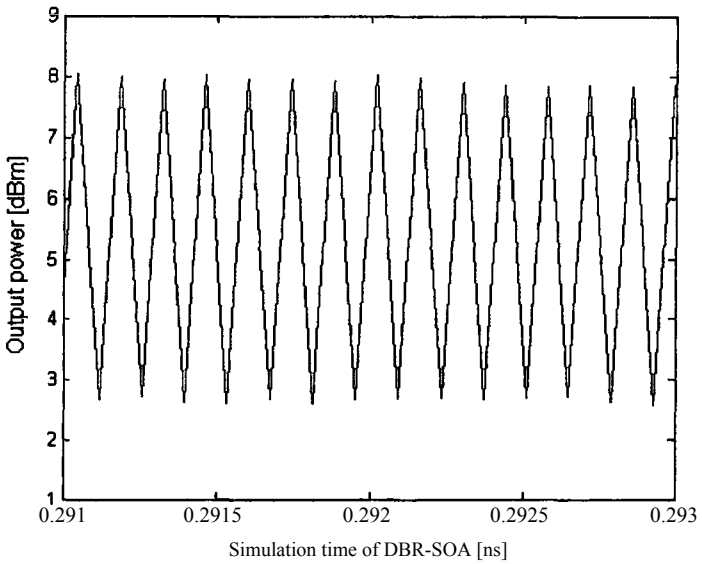

Fig. 5.4 Mode beating in lasing mode of DBR-SOA

The basic difference of DBR-SOA and TW-SOA is that the former is lasing when working but the latter is not. Therefore the bias currents through these two SOA's are different. In all figures of this section the DBR-SOA is pumped with an electronic current of 200 mA and the TW-SOA is pumped by 90 mA. It is assumed that 70% of the current passes through the active region. We also assume the input and output coupling losses are 3dB at the two facets, respectively.

The DC (Direct Current) signal coupled into SOAs is with a power of -25dBm. This DC signal is coupled into the two types of SOAs cavities 0.1 ns later after the start of simulation, respectively. During the 0.1 ns the device moves from a non-physical state, which is initialized with a set of estimated numerical values, into a somehow steady state, which makes physical sense. Figure 5.3 shows the output of amplified signal is a little bit later than 0.1 ns. This time delay is due to the propagation in device cavity. Figure 5.3(b) is the detail of lasing mode output in figure 5.3(a), which shows the mode beating. The mode beating is among different modes which beat in carrier rate equation. The beating period is about 0.14 ps.

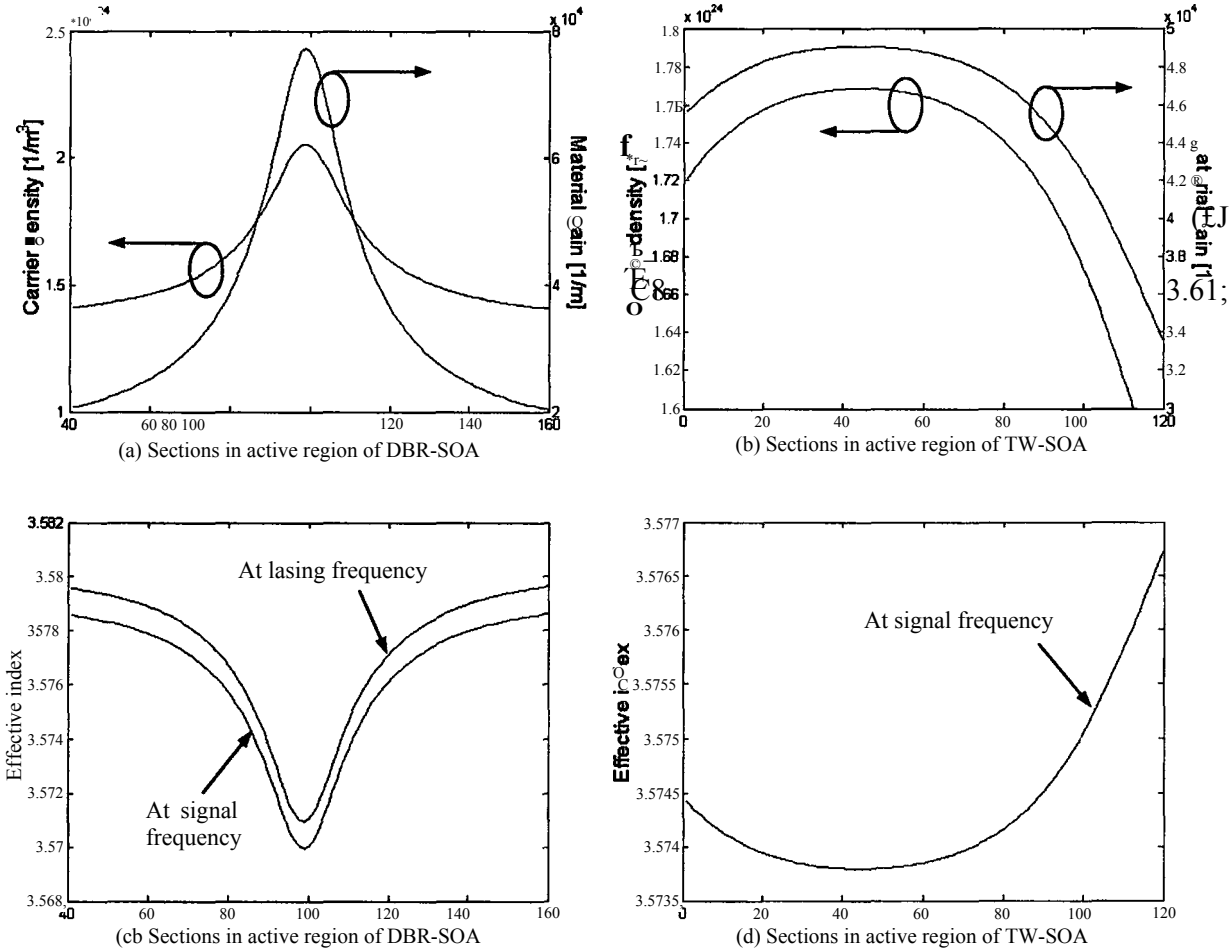

Bias current = 200 mA
Input signal power = -25dBm
Signal frequency = 1550 nm
Lasing frequency = 1530 nm

Bias current = 90 mA
Input signal power = -25 dBm
Signal frequency = 1550 nm

Fig. 5.5 Carrier density, material gain and effective index profiles of DBR-SOA and TW-SOA

After the two devices go into steady state, i.e., 0.5 ns after the start of simulation, some important data along cavities are recorded in figure 5.5, which verifies the correctness of the numerical simulation. The material gain and effective index are tightly related to carrier density, as shown in figure 5.5(a), in which the material gain and effective index are figured at signal wavelength 1550 nm. For both kinds of SOAs, the

larger carrier density is, the larger gain and smaller effective index are. But the difference between DBR-SOA and TW-SOA is also significant. In DBR-SOA the profiles of carrier density, material gain and effective index are nearly symmetric, because most of the carriers are contributed to lasing which is shown in figure 5.6. Compared to carrier recombination in lasing mode, the asymmetric carrier consumption in signal mode is too small and can be neglected. But in TW-SOA the asymmetric carrier consumption in signal mode is dominant over any other mode. This is sufficient to explain the asymmetric profile of TW-SOA.

The photon rates of signal, noise and lasing in device cavities are compared in figure 5.6. The figured noise photon rate is the sum of noise photon rates at all calculated noise modes. In order to obtain steady state photon rates, we average output photons over a time range of the last 1000 iterations.

In DBR-SOA the photon rates (also the photon densities) decrease in the DBR region because of the material loss. Figure 5.6 shows in DBR-SOA the photon rate in lasing mode is about -100 times larger than that of forward signal and/or total noise. That means lasing process is dominant in DBR-SOA. Since the DBR-SOA cavity is symmetric, the lasing process is also symmetric. Thus the cavity physical parameters, i.e., photon rates, carrier density, gain and effective index, are nearly symmetric along the longitudinal direction.

In TW-SOA the photon rate in signal mode is much larger (about 40dB) than that in any other noise mode, as shown in figure 5.7(b). Meanwhile, the total noise photon rate is about ~ 10^{10} times larger than signal photon rate. Figure 5.5(b) shows the carrier density in right half of the cavity is less than that in the left half. The relationship between photon rate and carrier density can be explained that, because the photon density in the right half is higher, it stimulates more recombination in the right half of the cavity than that in the left.

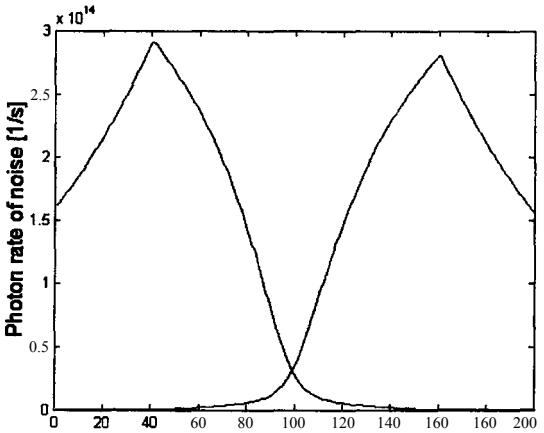

(a) Sections of DBR-SOA

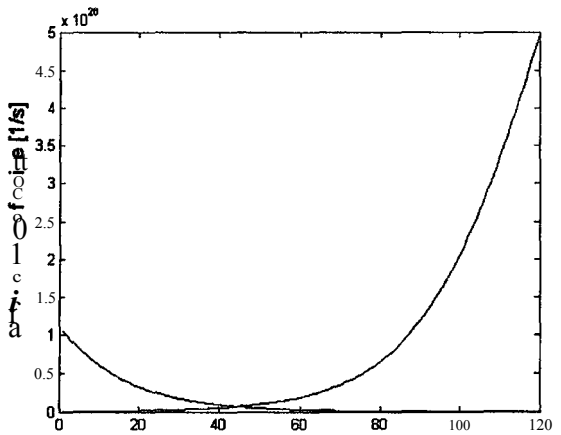

(b) Sections of TW-SOA

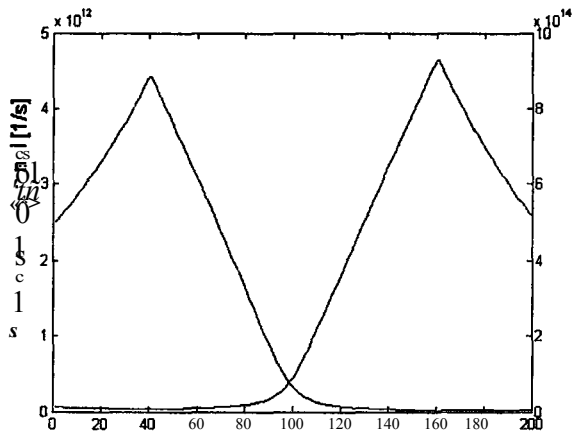

(c) Sections of DBR-SOA

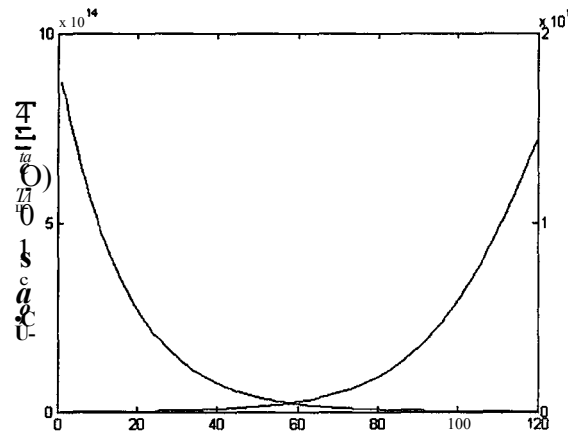

(d) Sections of TW-SOA

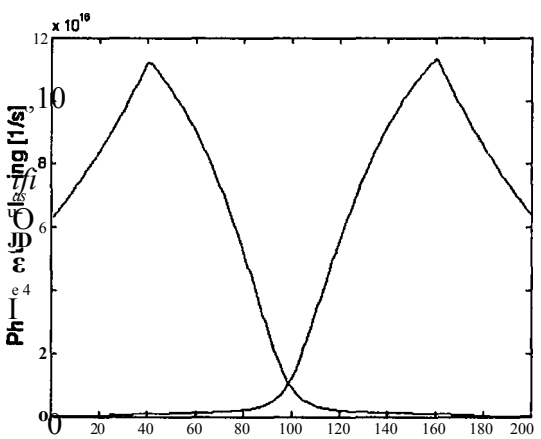

(e) Sections of DBR-SOA

Bias current of DBR-SOA = 200 mA
Bias current of TW-SOA = 90 mA
Input signal power = -25dBm
Signal frequency = 1550 nm
Lasing frequency = 1530 nm

Fig. 5.6 Photon rates of DBR-SOA and TW-SOA

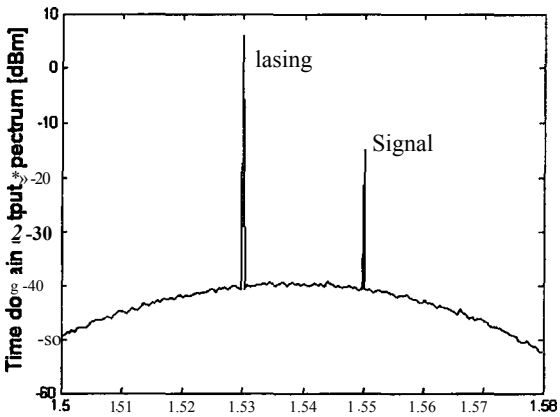

(a) Output wavelength of DBR-SOA [um]

Bias current of DBR-SOA = 200 mA
Input signal power = -25dBm
Facet power reflectivities = sxicr[5]

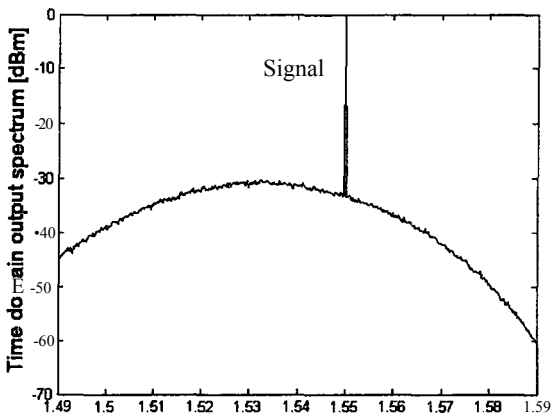

(b) Output wavelength of TW-SOA [um]

Bias current of TW-SOA = 90 mA
Input signal power = -25dBm
Facet power reflectivities = **5**xio~[5]

Fig. 5.7 Time domain power spectra of (a) DBR-SOA and (b) TW-SOA

In order to illustrate the optical output spectrum, the output signal and noise at the right facet is averaged at each wavelength over a time range of 300 iterations. Figure 5.7 is obtained with Eqs.(4.8) and (4.9). It should be noted the bias current to DBR-SOA is larger than that to TW-SOA because lasing process needs more pump. From this point of view we may say that a DBR-SOA is actually a DBR laser working with a signal input.

5.3 Dependence of Simulation Results on Simulation Parameters

Some non-physical phenomena and parameters are inevitably introduced to computer simulations. In this model three parameters should be investigated, which are spectral bandwidth, cavity discretization and frequency discretization. By properly choosing these parameters, a reasonable balance between simulation accuracy and time cost can be achieved.

5.3.1 Simulated Bandwidth

Obviously only a limited bandwidth can be covered by computer simulation, while Eq.(4.1) should be calculated on a bandwidth as wide as possible. Meanwhile, the wider the frequency range is covered, the more time the calculation costs. In order to exam how deeply the bandwidth will affect the accuracy of simulation result, a numerical experiment were conducted and the result is shown in figure 5.8.

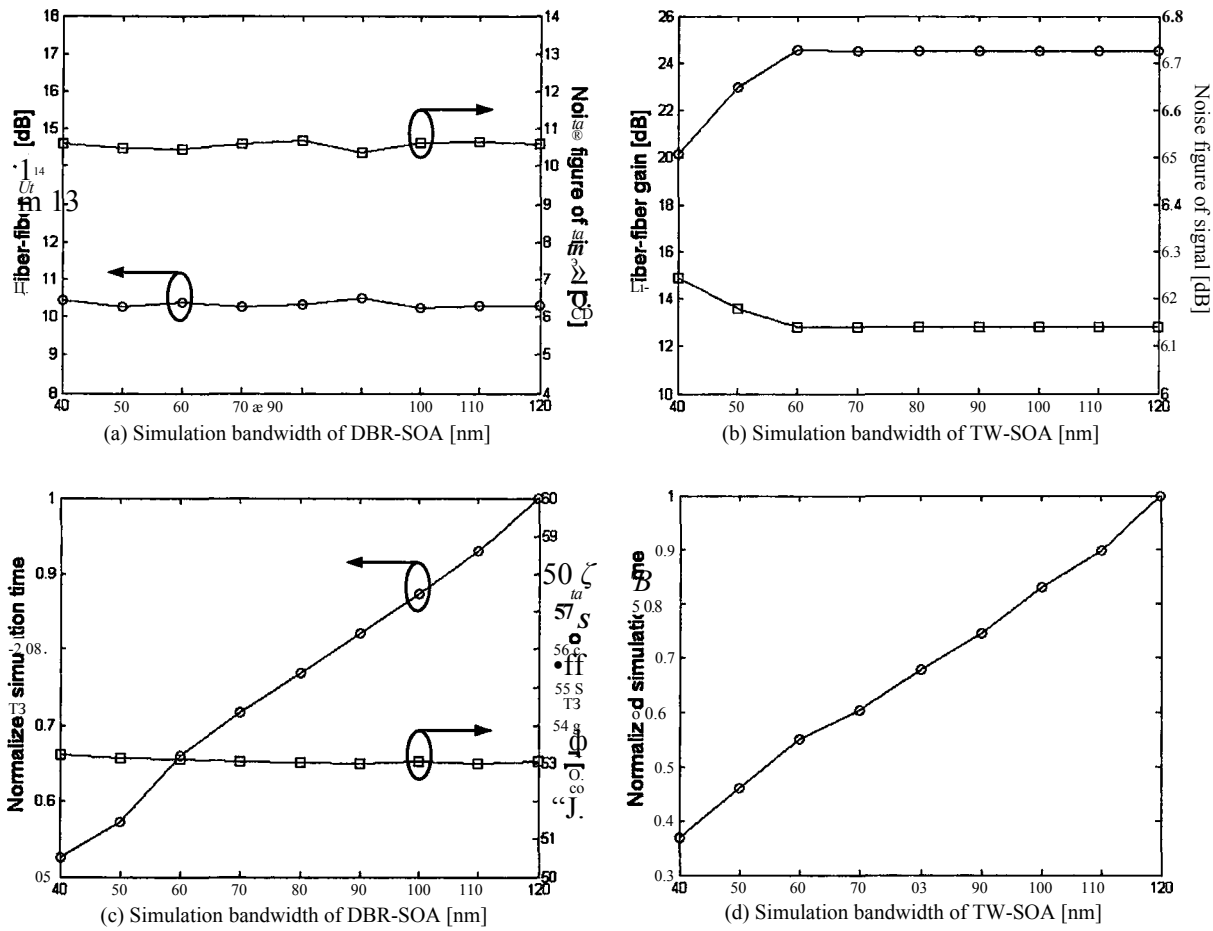

(a) Simulation bandwidth of DBR-SOA [nm]

(b) Simulation bandwidth of TW-SOA [nm]

(c) Simulation bandwidth of DBR-SOA [nm]

(d) Simulation bandwidth of TW-SOA [nm]

Fig. 5.8 Dependence on simulated bandwidth

In the numerical experiment, cavity and frequency discretization parameters are set to be conservative enough. Firstly, we evenly split the entire DBR-SOA along the longitudinal direction into 200 sections, in which 20 sections in each DBR region and 160 sections in active region. Similarly the TW-SOA is split into 160 sections and each section is with a length equal to that of the DBR-SOA for comparison purpose. By this way, the cavity discretizations in the active regions of DBR-SOA and TW-SOA are identical. Secondly, frequency discretizaion factor is $K_d = 1$ so that the error introduced by frequency discretization is eliminated. It is proved in Section 5.3.2 and 5.3.3 that the above settings are conservative enough to remove the affection of cavity and frequency discretizations.

Figure 5.8 shows the experiment result which covers the bandwidth range from 40 nm to 120 nm. The figure clearly shows that the time cost of simulation is linearly proportional to the simulated bandwidth. In DBR-SOA, the fiber-to-fiber gain, noise figure and lasing output power are not sensitive to simulated bandwidth. The root course is that the carrier recombination contributed to lasing and/or signal amplification is much more than that contributed to ASE noise, as shown in figure 5.6(a). Thus the calculated bandwidth of ASE noise has almost no effect on the simulation result of DBR-SOA. In the TW-SOA, the fiber-to-fiber gain and noise figure are virtually independent on the simulated bandwidth after the bandwidth is wider than 60 nm. This difference from DBR-SOA is because in TW-SOA the signal photon rate is less than the total noise photon rate although it is much larger than that in any single noise mode. Therefore there must be certain threshold bandwidth beyond that the photons in noise modes can be neglected. This is demonstrated in figure 5.7(b).

It should be noted that the bandwidth must be properly selected so that the peak area of the gain is covered in the simulation. In all the following simulations the bandwidth is chosen to be 80 nm.

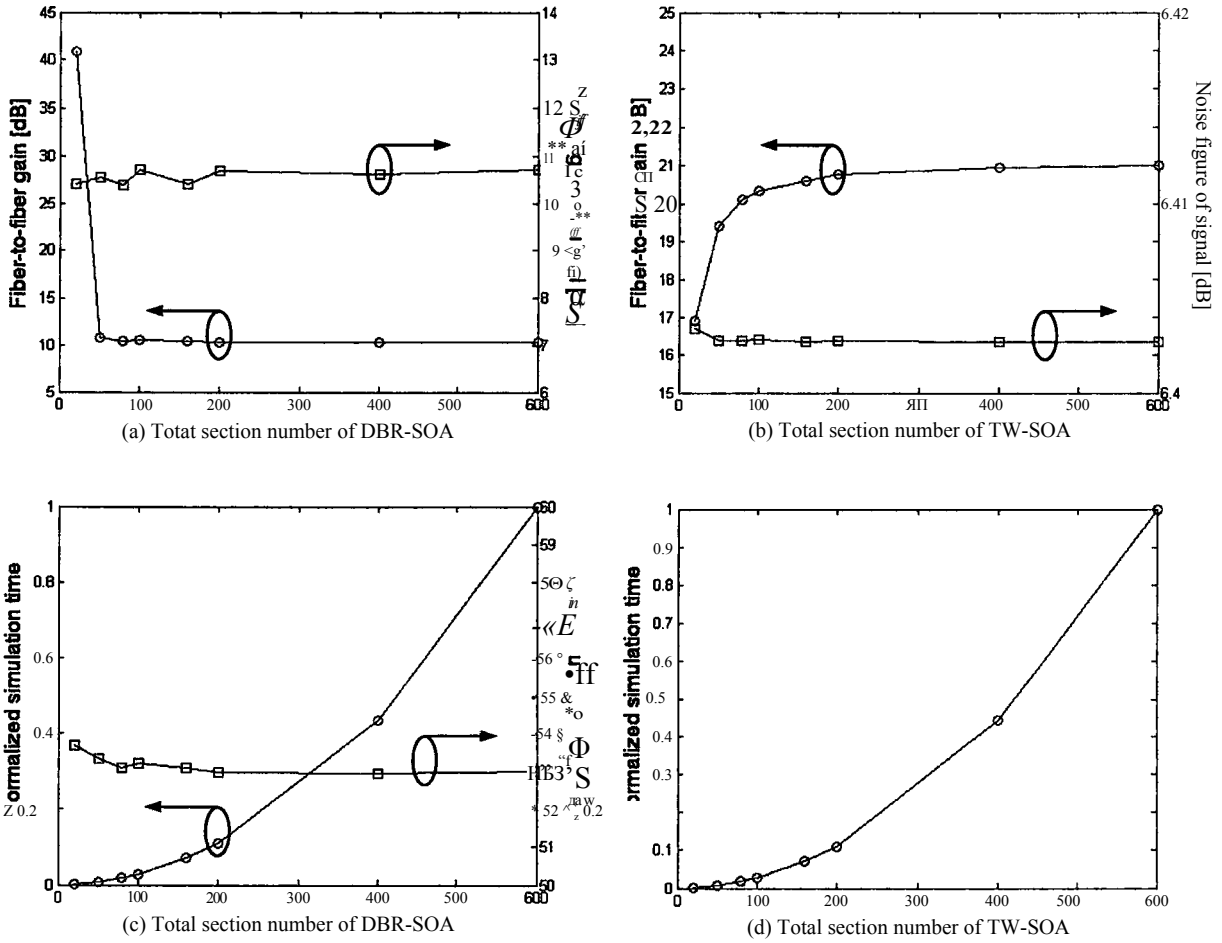

Fig. 5.9 Dependence on cavity discretization

5.3.2 Cavity Discretization

The wave equations are solved by the numerical algorithm Eq.(4.1), which is based on the split of the cavity. The more sections we split the cavity, the more accurate the solution we could get, and the more time cost we have to pay. In order to balance the solution accuracy and time cost, a numerical experiment was conducted. This experiment covers the range of total section numbers from 20 to 600. To make sure the result is

reliable, the simulated bandwidth is 80 nm and no frequency discretization is applied, i.e., frequency discretizaion factor K_d = 1. The experiment result, figure 5.4, shows that when the section number is larger than 200, the fiber-to-fiber gain, noise figure and lasing output power become independent on cavity discretization in both DBR-SOA and TW-SOA, while the time cost increases nonlinearly. Therefore we choose 200 as the section number in the following simulations.

5.3.3 Frequency Discretization

Frequency discretizaiton is used to reduce the simulation time cost which is described by Eq.(4.6). We use numerical experiment to estimate the impact of frequency discretization factor K_d, which denotes how many cavity modes are combined together to be calculated by a single wave equation. In this experiment the value of K_d covers the range from 1 to 30, as shown in figure 5.10. The result is interesting, which shows that the fiber-to-fiber gain, noise figure and lasing output power are all not very sensitive to the value of K_d in both DBR-SOA and TW-SOA. This is the evidence that the error introduced by frequency discretization can be neglected, because the majority of optical carrier combinations are contributed to signal amplification and/or lasing process. On the other hand, when K_d starts to increase from K_d =1, the simulation time cost heads down greatly, but after K_d is larger than 10 the time cost will change very little. This is because the simulation time for frequency domain only occupies a little part of the whole simulation time when K_d is larger than 10. Therefore we choose K_d =10 in the following simulations.

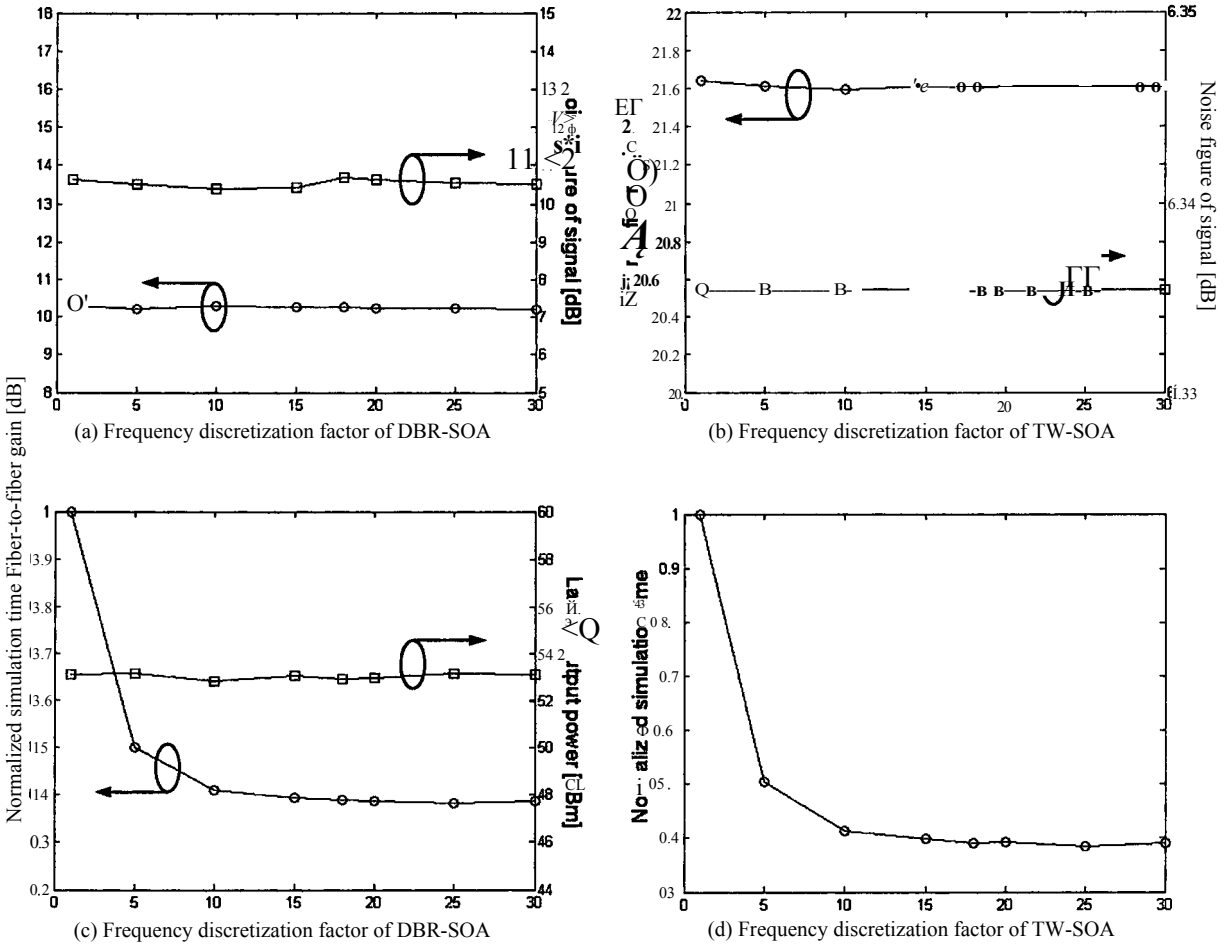

(a) Frequency discretization factor of DBR-SOA

(b) Frequency discretization factor of TW-SOA

(c) Frequency discretization factor of DBR-SOA

(d) Frequency discretization factor of TW-SOA

Fig. 5.10 Dependence on frequency discretization

CHAPTER 6
DEVICE PERFORMANCE SIMULATION

The performance dependence on working conditions and device structure of these two types of SO As is simulated in this chapter. It covers input optical power, bias current, saturation output power, cavity length.

6.1 Input Optical Power

Figure 6.1 shows the device behavior with different input signal power. In DBR-SOA, with the increase of input optical signal power, the output signal power increases linearly and the output lasing power decreases linearly, as shown in figure 6.1(a). In this region the fiber-to-fiber gain of DBR-SOA is clamped to a constant about 10.05 dB. When the input signal power exceeds a threshold, around 0.5mW in figure 6.1(a) and/or -3dBm in figure 6.1(b), the fiber-to-fiber gain saturates and drops rapidly meanwhile the output lasing power shrinks. In TW-SOA, when the input signal power is very small, i.e., less than -30 dBm, the fiber-to-fiber gain is also nearly constant, about 21 dB in figure 6.1(d). This is because when the input signal power is very small, the variation of input signal can not affect the distribution of carrier density. But with the further increase of input signal power, the fiber-to-fiber gain decrease gradually to saturation region and there is not an obvious threshold value.

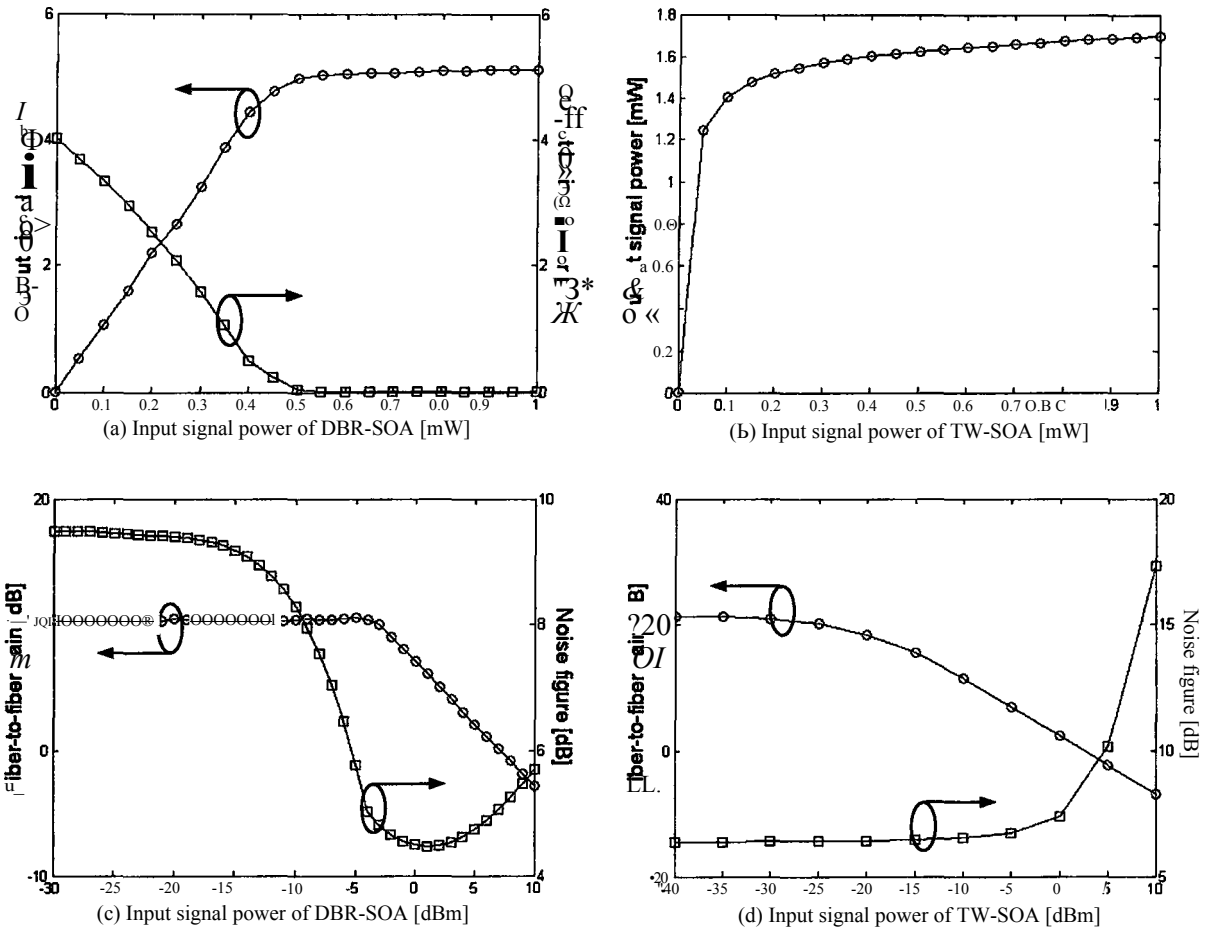

Fig. 6.1 Performance dependence on input optical power
(Bias of DBR-SOA = 200 mA, Bias of TW-SOA = 80 mA)

In the gain-clamped region of DBR-SOA, the noise figure decreases with the increase of input signal power. This is because the increase of input optical power has a tendency to redistribute the carrier density so that the peak of carrier density shifts from the center of the cavity to the input end, as shown in figure 6.2(a), meanwhile the total injection carrier density keeps constant. According to Eq.(4.16), the noise figure of SO A mostly depends on the first several sub-sections. When the peak of carrier density shifts to certain point, about 0 dBm in our experiment, the minimum noise figure is obtained. With the further increase of input optical power, the carrier is squeezed to the input end,

and the device moves into a gain saturation state in which the device noise figure starts to go up.

The noise figure curves of TW-SOA looks quite different from that of DBR-SOA. Because there is no lasing in the cavity, the carrier density concentrates on the input end, as shown in figure 6.2(b). With the increase of the input power, this tendency is enhanced. The larger the carrier density is, the more carrier recombinations occur. This happens in the first several sub-sections that dominates the total noise figure. With Eq.(4.16), it is easy to understand the rising curve of noise figure in figure 6.1(d).

6.2 Bias Current

Similar to electronic transistors, SOA's behavior depends on bias currents. On the other hand, the power of input optical signal also plays a role to determine the physics of devices, i.e., a large input optical signal pushes the device into a saturated gain regime while a small input signal makes the device operating in an unsaturated gain regime. These two cases are discussed in the following sections respectively.

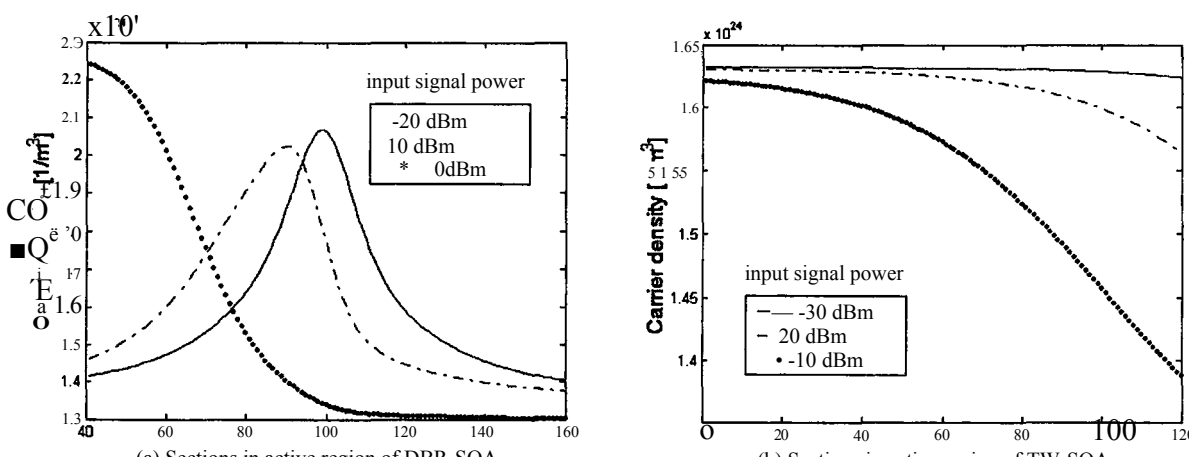

(a) Sections in active region of DBR-SOA

(b) Sections in active region of TW-SOA

Fig. 6.2 Carrier density distribution with different input signal power

6.2.1 Dependence on Bias Current with Small Input Signal

In DBR-SOA, as the input signal power is small, the device works in an unsaturated regime and the gain is clamped, as shown in figure 6.1(a). When the bias current is larger than about 130 mA, as shown in figure 6.3(a,c), the DBR-SOA starts lasing and moves into a clamped-gain state in which the fiber-to-fiber gain is virtually independent with the bias current. On the other hand, the noise figure and lasing output power arise with the increase of bias current.

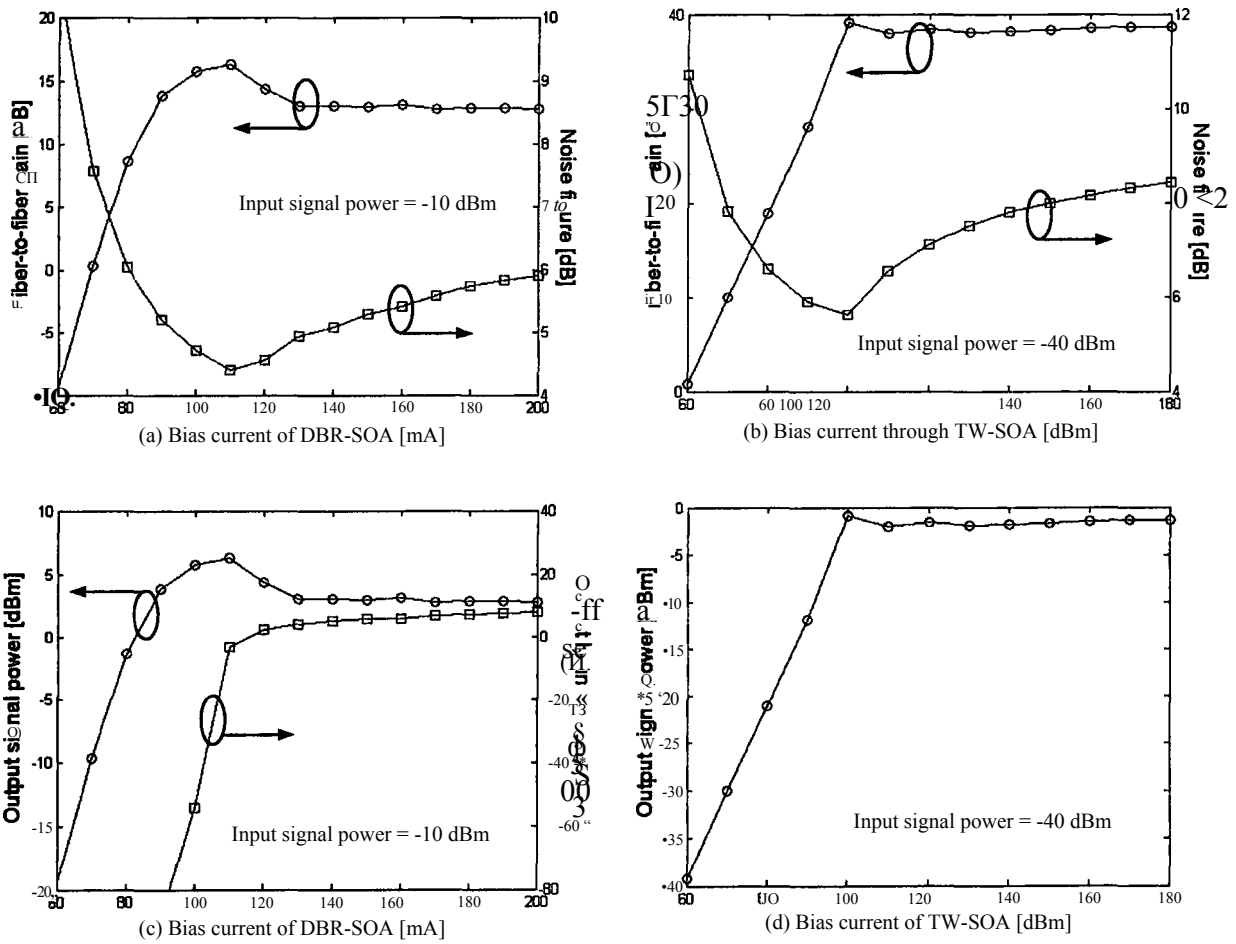

(a) Bias current of DBR-SOA [mA]

(b) Bias current through TW-SOA [dBm]

(c) Bias current of DBR-SOA [mA]

(d) Bias current of TW-SOA [dBm]

Fig. 6.3 Dependence on bias current with small signal input (unsaturated)

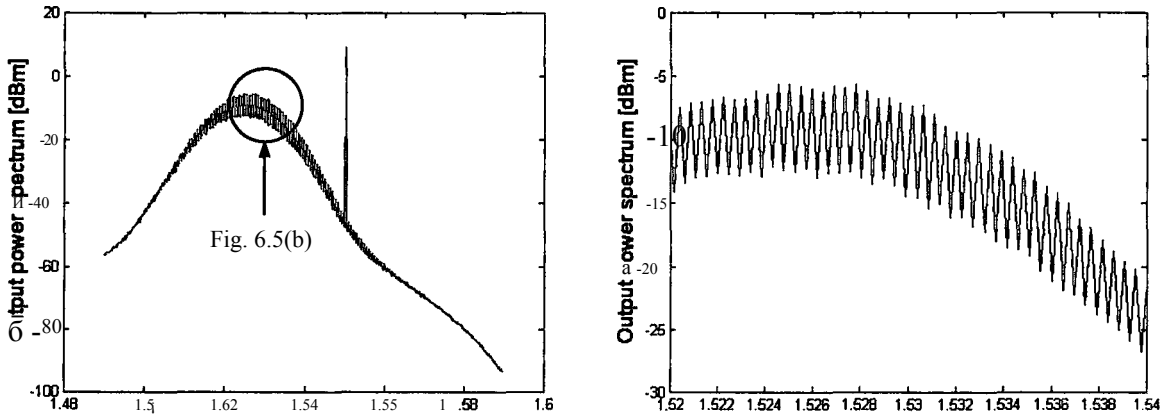

Fig. 6.4 Output spectrum of TW-SOA (Bias current = 180 mA, Input signal power = -40 dBm)

In TW-SOA, the fiber-to-fiber gain is proportional to the bias current when the bias is less than 100 mA, as shown in Fig6.3(b). Because there is not lasing in TW-SOA, the increase of bias current results to an increase of gain, while the noise figure drops down. After the bias is larger than 100 mA, the gain of TW-SOA is also clamped to a maximum value, because with the huge bias currents TW-SOA behaves like a FP-laser. This is demonstrated in its output spectrum. Figure 6.4(a) shows a bunch of noise modes is actually lasing, whose detail is shown in figure 6.4(b). This is very similar to DBR-SOA thereby a similar gain-bias curve is observed. The only difference is that the lasing occurs in the modes determined by the wavelength of gain peak rather than DBR wavelength. However its effect to gain dynamics is quite same with that of DBR-SOA.

6.2.2 Dependence on Bias Current with Large Input Signal

When the input optical signal is larger than a threshold, SOAs work in the gain saturation regime, where the fiber-to-fiber gain drops more than 3dB from the small signal gain. At this threshold, the output signal power is termed by output saturation power. According to figure 6.1, 0.8 mW and -10 dBm are selected as the input signal power of DBR-SOA and TW-SOA respectively in the following experiment.

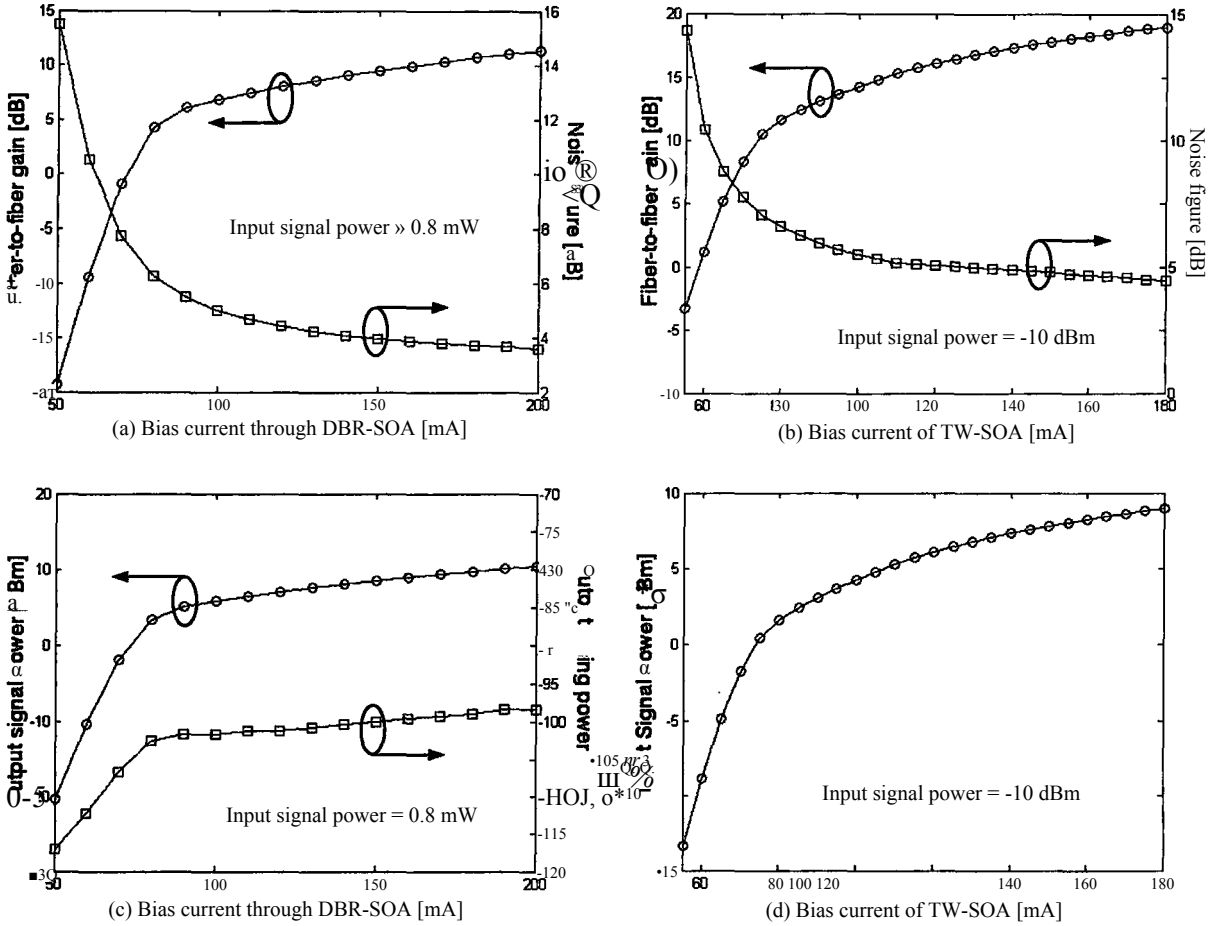

(a) Bias current through DBR-SOA [mA]
(b) Bias current of TW-SOA [mA]
(c) Bias current through DBR-SOA [mA]
(d) Bias current of TW-SOA [mA]

Fig. 6.5 Dependence on bias current with large signal input (saturated)

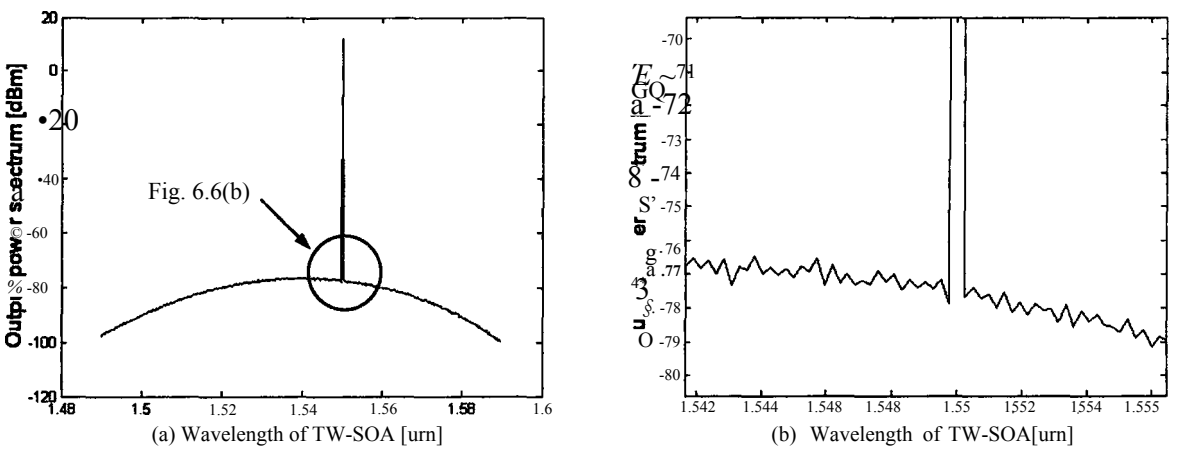

(a) Wavelength of TW-SOA [urn]
(b) Wavelength of TW-SOA[urn]

Fig. 6.6 Output spectrum of TW-SOA (Bias current = 180 mA, Input signal power = -10 dBm)

Figure 6.6 shows the fiber-to-fiber gain and noise figure curves of DBR-SOA and TW-SOA looks quite similar when they are working with large input signal powers. When bias currents increase, the fiber-to-fiber gains keep on going up and noise figures drop. Besides, the output lasing power of DBR-SOA also arises with the increase of bias. The only difference is that the DBR-SOA needs a more powerful input signal than that of the TW-SOA needs to drive them into gain saturation regime.

In TW-SOA, different from the scenario of small signal input, a large bias current, e.g., 180mA, can not push the device to lase in noise modes, as shown in figure 6.6, because a huge number of carriers have been consumed by amplifying the large input signal.

6.3 Output Saturation Power

Output saturation power is an output signal power with that the device gain is 3dB less than its value when the input signal power is very small, or say, the device gain is 3dB less than the unsaturated gain. Figure 6.7 shows the output saturation powers of DBR-SOA and TW-SOA verse different bias currents.

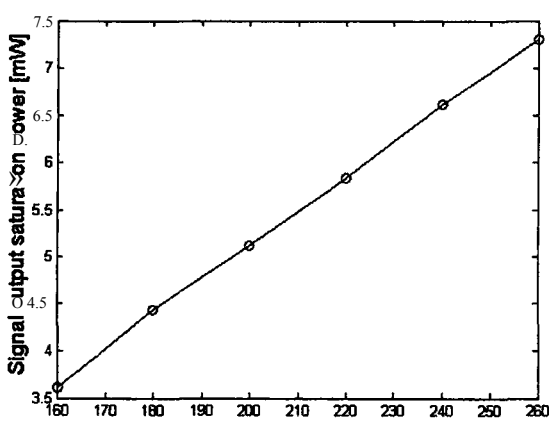

(a) Bias current through DBR-SOA [mA]

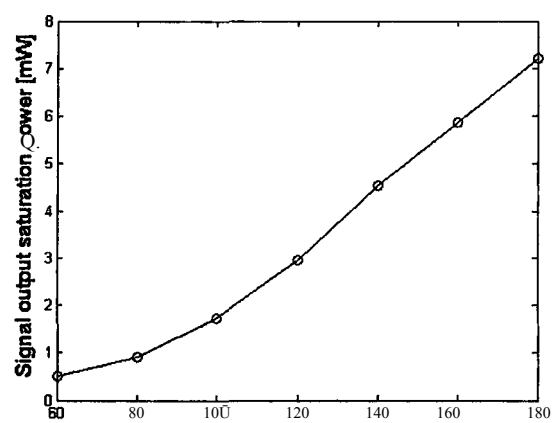

(b) Bias current through TW-SOA [mA]

Fig. 6.7 Output saturation power

Output saturation power is an important parameter of a SOA because it indicates the maximum output signal power that a SOA can produce with a relatively constant gain. This is desired in many communication systems. Figure 6.7 shows the output saturation power of DBR-SOA is linearly proportional to the increase the bias. When the bias is larger than about 100mA, TW-SOA also shows the same characteristic. It should be noted that a DBR-SOA usually works with a bias whose range is shown in figure 6.7(a), because a large bias is required to make the device lasing. However, a TW-SOA usually works with a small bias, e.g., less than 100mA as shown in figure 6.7(b), because a large bias will drive the noise modes start lasing. These lasing modes can not be properly controlled by a FP cavity so that it will add too much noise to communication cannels, especially in WDM system.

6.4 Dependence on Cavity Length

In above sections we discussed the performance dependence on working conditions. Actually the device dimensions and structure parameters also determine the performance. Coupling coefficient and the lasing wavelength is the major structure parameters of DBR-SOA, which is investigated in [10]. Here we just compare the effect of cavity length on DBR-SOA and TW-SOA. The simulations are grouped into two sets, one with a constant bias current (mA), the other with a constant bias intensity (mA/mm). The simulation results are listed in Figs.6.8 and 6.9, respectively. All simulations are with an input signal power of - 25 dBm.

When the bias currents are kept as constant, i.e., 200mA to DBR-SOA and 80mA to TW-SOA, the DBR-SOA with a longer cavity has a larger fiber-to-fiber gain, as what we expected. On the contrary TW-SOA with a longer cavity has a smaller fiber-to-fiber gain when the bias current is a constant, as shown in figure 6.8(a) and (b). The reason is, with a constant bias, the longer the cavity, the lower the carrier density is. Therefore the output lasing power of DBR-SOA is lower. But the amplified field increases exponentially along

longitudinal direction, thus the signal output power is larger with the longer cavity length. In TW-SOA, with a lower carrier density, the device gain is lower. The noise figure of DBR-SOA rises gradually with the increase of cavity length, while the noise figure of TW-SOA rises rapidly when cavity length is longer than 600 $\mu\pi$\.

When the bias intensities are kept as constant, i.e., 233 (mA/mm) to DBR-SOA and 93 (mA/mm) to TW-SOA, as shown in figure 6.9, the fiber-to-fiber gains of both SOAs rise with the increase of cavity length. It is interesting that the increment of cavity length leads to only very limited increment of noise figure in TW-SOA.

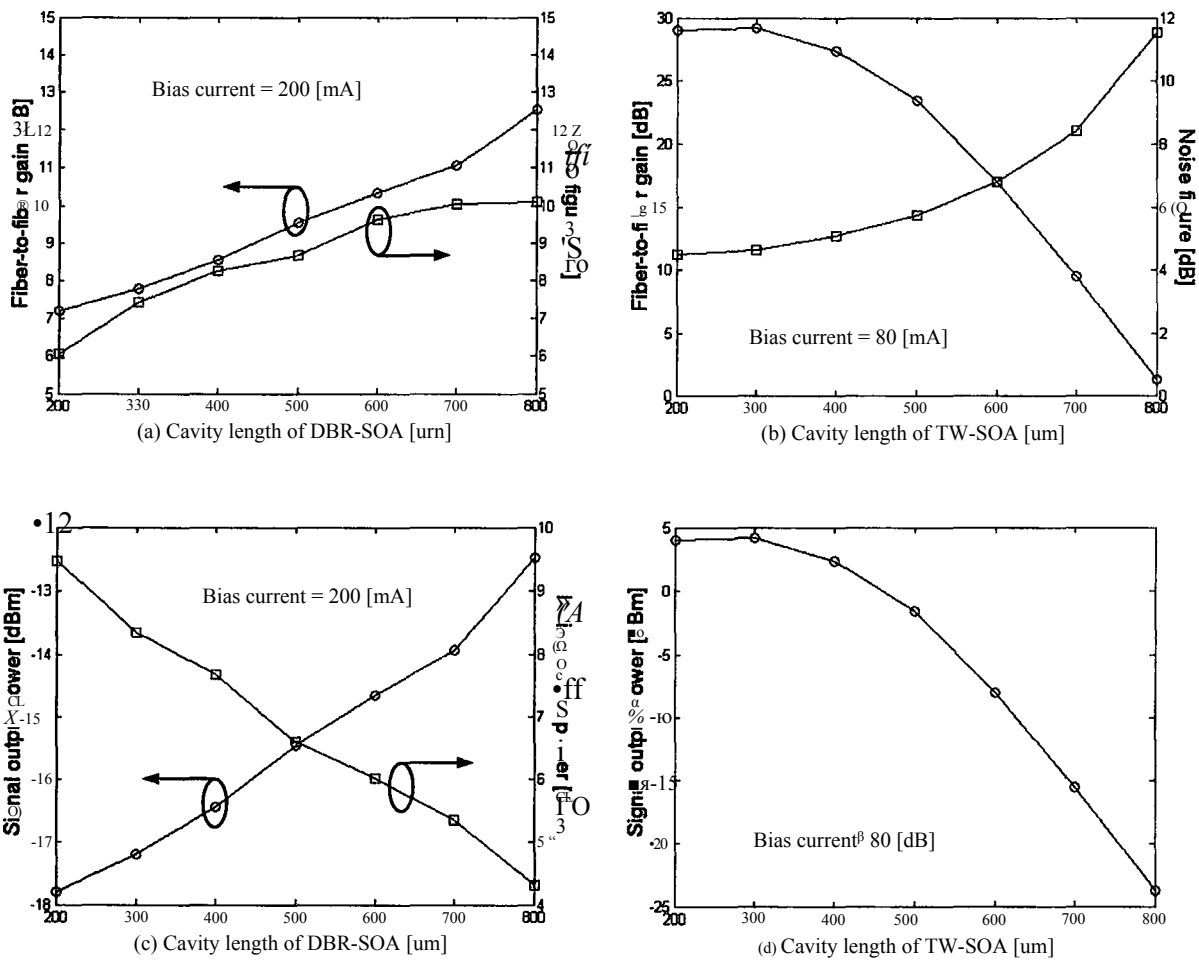

(a) Cavity length of DBR-SOA [urn]

(b) Cavity length of TW-SOA [um]

(c) Cavity length of DBR-SOA [um]

(d) Cavity length of TW-SOA [um]

Fig. 6.8 Performance comparison with different cavity lengths (constant bias current)

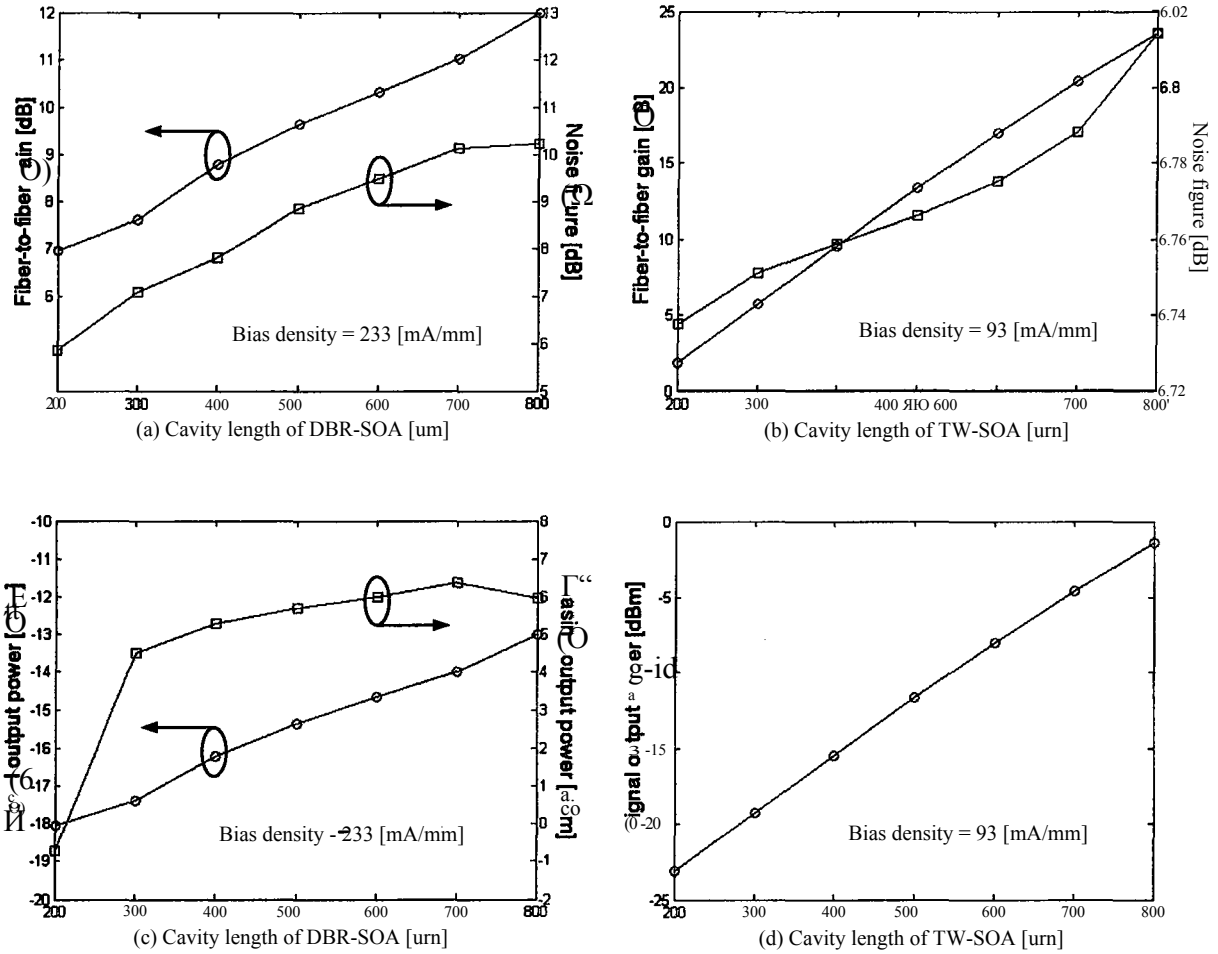

(a) Cavity length of DBR-SOA [um]

(b) Cavity length of TW-SOA [urn]

(c) Cavity length of DBR-SOA [urn]

(d) Cavity length of TW-SOA [urn]

Fig. 6.9 Performance comparison with different cavity lengths (constant bias intensity)

In DBR-SOA, no matter constant bias current or constant bias density, the effect of cavity length on device gain and noise figure is nearly same. But in TW-SOA this effect is different. The root cause of this difference is the lasing mechanism in DBR-SOA.

CHAPTER 7
EXAMPLES OF APPLICATION

Three application examples are given in this chapter. The benefit of gain-clamped SOA in WDMA system is demonstrated. The non-linear application of TW-SOA as a wavelength converter is also shown.

7.1 An Example of Amplified NRZ Code

As an example of linear amplification, a NRZ (None-Retum to Zero) code flow is coupled into a DBR-SOA (Bias current = 200 mA) and a TW-SOA (Bias current = 80 mA), respectively. The input, output and the reflected signal are shown in figure 7.1. The input signal itself has no noise (ideal digital code). All noise in output signals comes from SOAs. When the input signal power is small, i.e., -40 dBm for bit 0 and -30 dBm for bit 1, as shown in figure 7.1(a) and (b), the only difference of the two SOAs is that the fiber-to-fiber gains of DBR-SOA and TW-SOA are different, about 10 dB and 23 dB for each one respectively. When the input signal power is large, i.e., -15 dBm for low level and -10 dBm for high level, as shown in figure 7.1(c) and (d), the fiber-to-fiber gain of DBR-SOA is still 10 dB while the fiber-to-fiber gain of TW-SOA drops to 13 dB. The effect of gain saturation in TW-SOA is very obvious. It should be note that the input signal is coupled in at only a single wavelength channel in this simulation. The reflected signal toward reward direction is also shown in figure 7.1.

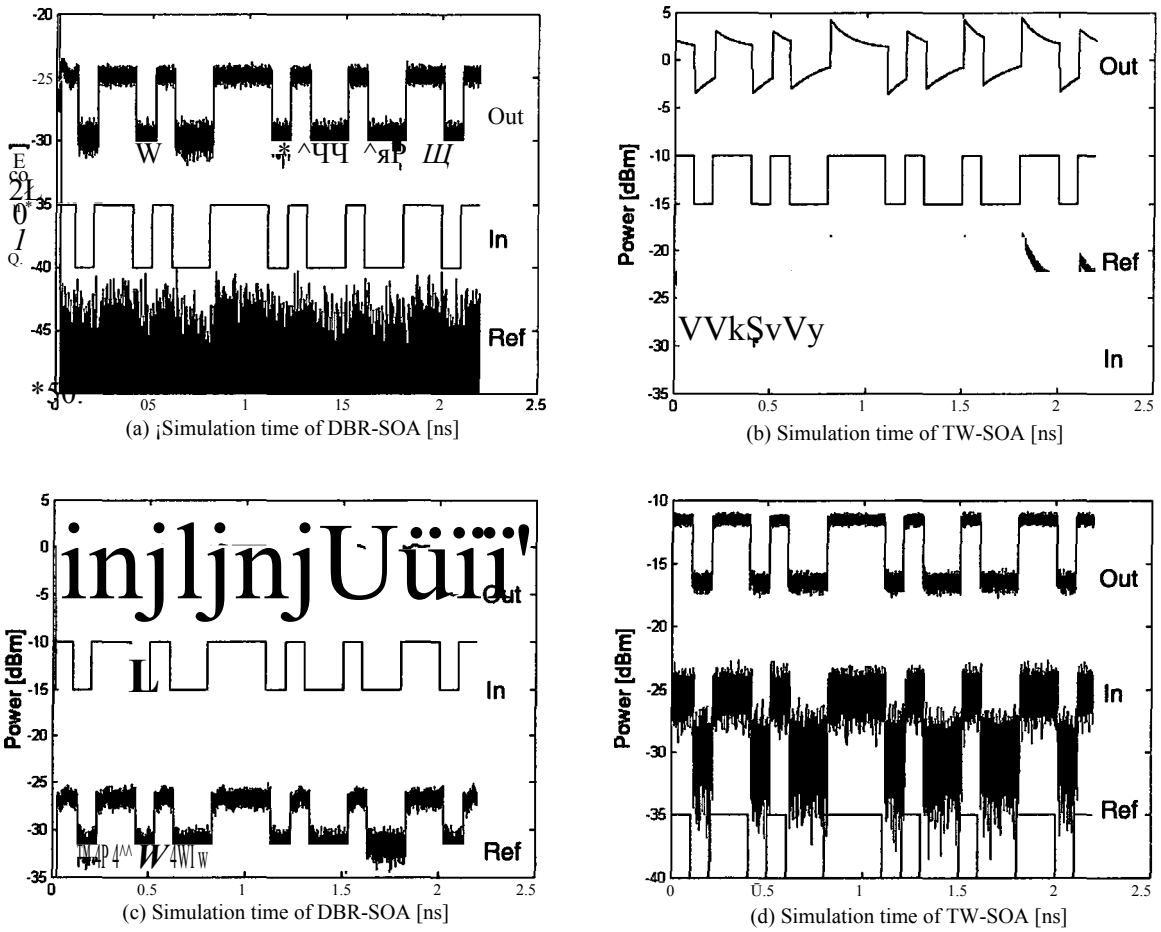

In — Input signal Out—Output signal Ref — Reflected signal

Fig. 7.1 Amplified NRZ data

7.2 Amplification in a WDM System

In a Wavelength Division Multiplexing (WDM) network, the input optical power varies with the number of total wavelength channels. A constant fiber-to-fiber gain, which is independent on input optical power, is critical for a stable system performance. Therefore the GC-SOA has an important application in WDM systems. To demonstrate the

significance of the clamped gain, the performances of a DBR-SOA and TW-SOA in a WDM system are compared in the following.

Bit Error Rate (BER) is one of the key parameters to measure the performance of a digital transmission system. It is acceptable to assume the occurrence probabilities of bit 0 and 1 are equal, and the statistics of finally received data are Gaussian, which has counted for all noise and errors in the process of optical amplification, optoelectronic conversion, and data sampling. With an optimum design of optoelectronic receiver [38], BER can be calculated by

$$BER = \frac{1}{2}\operatorname{erfc}\left(\frac{Q}{\sqrt{2}}\right)$$
$$Q = \frac{I_1 - I_0}{\sigma_1 + \sigma_0} \tag{7.1}$$

where I_1 and I_0 are the average values of bit 1 and bit 0, respectively; σ_1 and σ_0 are the standard deviations of bit 1 and bit 0, respectively.

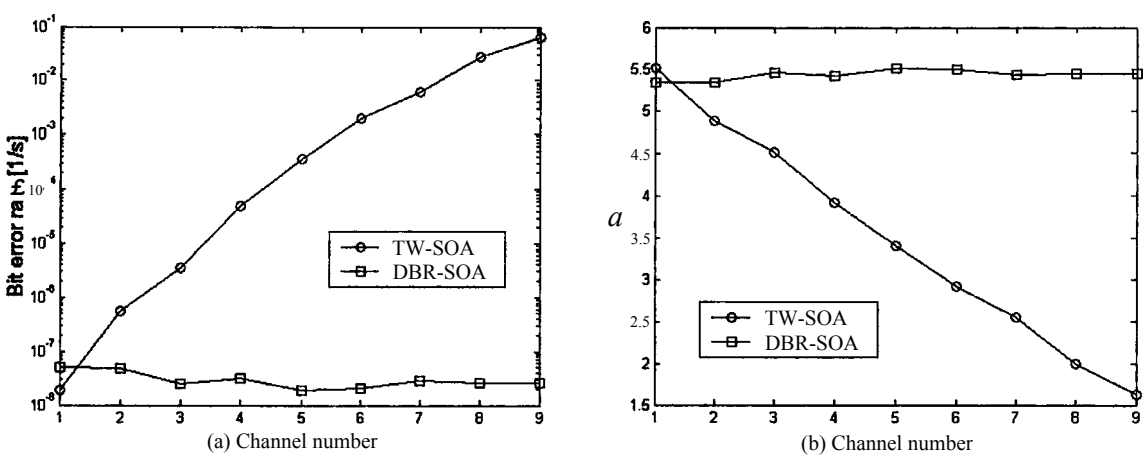

Fig. 7.2 BER and Q of DBR-SOA and TW-SOA in WDM system

Some simulation parameters are listed below.

Bias current	**200 mA (DBR-SOA)**	**80mA (TW-SOA)**
Input signal power	**-25 dBm (bit 1)**	**-30dBm (bit 0)**

Wavelengths of 9 channels *(jum)*

1.5467 1.5471 1.5476 1.5481 1.5486 1.5490 1.5495 1.5500 1.5558

Figure 7.2 is the simulation result. The x-axis is the number of total signal channels used in WDM system. Figure 7.2(a) shows the BER of TW-SOA grows up greatly with the increase of the WDM channels, while the BER of DBR-SOA is independent on the variation of channel number. The Q, shown in figure 7.2(b), has the similar result. The degraded BER of TW-SOA is due to the crosstalk among WDM channels, because the optical power in one channel make the gain fluctuated and thereby interfere the data in other channels. On the contrary, the gain of DBR-SOA is clamped by lasing mechanism, thus the inter-channel crosstalk due to gain fluctuation is minimized.

Figure 7.2 is obtained with Eq.(7.1). It should be noted that this approach is not strict to calculate BER in our case. But it is good enough to demonstrate the relative relationship between BER and channel number.

7.3 Wavelength Converter

Wavelength converter plays an important role in all-optical networks [19, 20, 25]. It converts optical signal from one wavelength to another without optoelectronic conversion. Gain saturation in TW-SOA can be utilized to implement wavelength conversion, which is termed by cross gain modulation (XGM).

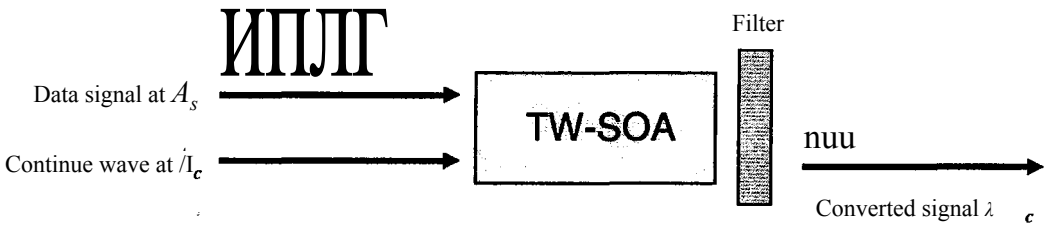

Fig. 7.3 XGM wavelength converter

Figure 7.3 is the configuration of XGM wavelength converter in our simulation. The digital signal modulated at wavelength $\mathring{A}_s$ is coupled into a TW-SOA. At the same end a DC optical signal at wavelength A_c is coupled in. If the total optical power makes the TW-SOA working in a saturation state, the high/low (1/0) optical power at wavelength $\tilde{A}_s$ modulates the carrier density and device gain, so that the output optical signal at wavelength $Л_c$ is modulated by the data.

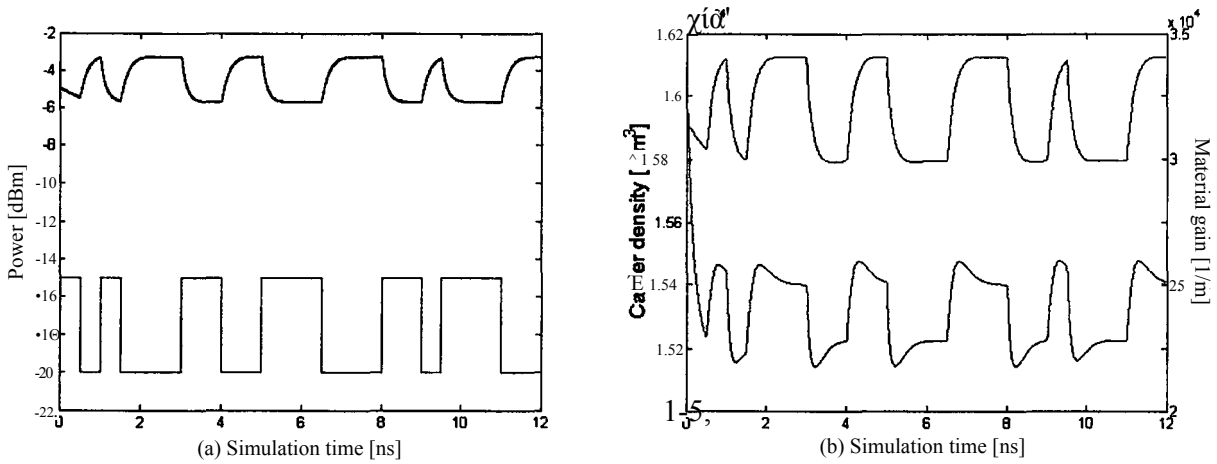

Fig. 7.4 Simulation result of XGM wavelength converter

Figure 7.4 is the simulation result. The input DC signal (continue wave) is with an optical power of - 20 dBm. The DC signal and digital signal should have optical powers on the same order. Figure 7.4(b) shows the carrier density and material gain are modulated by input data. Figure 7.4(a) shows the output converted signal has a reversed phase. And the distortion is obvious which is due to the time delay from the high-low power switch to the extinction and accumulation of carriers.

CHAPTER 8
CONCLUSIONS OF PART I

We theoretically studied the transient behaviors of GC-SOA and TW-SOA through a dynamic model. This model consists of a distributed feedback wave equation, a carrier rate equation and a material gain model, thereby can be used to simulated both GC-SOA and TW-SOA. DBR-SOA is one of the several structures of GC-SOA. With this model, we simulated a DBR-SOA and a TW-SOA. In order to compare their performances, the two devices have same material and structure in the active regions. Three important non-physical parameters, simulated bandwidth, cavity discritization and frequency discretizaiton, are evaluated to balance the time cost of simulation and the accuracy of the result.

The performance comparison is discussed in Chapter 6. Compared to TW-SOA, DBR-SOA has a very stable device gain which is independent on input optical power, and even not very sensitive to bias current if with a small input signal. From a noise level point of view DBR-SOA and TW-SOA have different characteristics. In system applications we can accordingly set the working condition to obtain a low noise level. Some application examples are presented in Chapter 7, which indicates that GC-SOAs are more suitable for linear amplification, while TW-SOAs are very potential in non-linear applications.

SOA has a brilliant perspective in fiber-optic communications. Its very compact dimensions and very simple structure imply the low cost and the potential for integration

on a single chip with other devices. Based on this thesis there is a lot of works waiting for further research.

Firstly, a more advanced model is required to cover more physics. For example, the model used in this thesis does not cover mode coupling. Therefore some non-linear physics such as Four-Wave Mixing (FWM) can not be simulated with this model. Besides, a 3-D model is necessary for a deep research of the device physics. With a more advanced model the characteristic of SOA can be emulated to a better degree so that the device design can be optimized.

Secondly, parameter abstraction is a key issue. Besides some structure parameters, lots of physical parameters have been used in this model and/or any other models. With limited data which is measured in lab experiment, how to abstract all the desired physical parameters is a valued research.

These works should be focused in our future research.

CHAPTER 9

INTRODUCTION OF PART II-------

IMPACT OF DISPERSION ON HYBRID OF FREQUENCY-HOPPED OPTICAL CDMA AND WDMA NETWORKS

The hybrid of frequency-hopped optical code-division-multiplexing access (CDMA) and the wavelength-division-multiplexing access (WDMA) combines the benefits of the vast bandwidth offered by the optical fiber and the flexibility of the CDMA access schemes. By using the CDMA technique, the multiple access function is performed not by wavelength selection, but by code-match-filtering [43-46]. Consequently, tunable transmitter and receiver are replaced by optical encoder and decoder, respectively. Further, the number of channels that can be accommodated by the system will not be limited by the number of wavelengths.

A number of different OCDMA methods have been proposed, including *direct sequence, time hopping,* and *frequency hopping* [45, 46]. In the follow chapters, we will concentrate only on the *frequency hopping* scheme, in which the carrier wavelength is shifted periodically according to a certain pre-assigned code. This situation differs from the WDMA in the sense that a fixed wavelength is not assigned to a given channel. Rather, all channels share entire bandwidth by using different carrier wavelengths at different time slots according to a code. In this system, each user is assigned a unique frequency-hopping pattem (or code) to ensure that any two users do not transmit at the same wavelength during a same time slot. This means the code sequences is strict orthogonal. Therefore the multiple access interference (MAI), which is the most important noise source in most CDMA systems, is theoretically minimized to zero.

Understandably, one of the major issues for this scheme is the effect of the fiber dispersion. Since a broadband optical source is used, each carrier wavelength will propagate with a different group velocity and consequently arrive at the receiver asynchronously. On the other hand, synchronization between the transmitter and receiver is required by CDMA decoding. It is therefore necessary to analyze the impact of the fiber dispersion on the system performance based on realistic system parameters. This paper is organized as follows: the system architecture is described in Chapter 10 and the power penalty due to dispersion is modeled in Chapter 11 by comparing the Q only with crosstalk and the Q with both crosstalk and dispersion. The simulation results are presented in Chapter 12 for the power penalties with different number of wavelength channels, channel wavelength spacing, and fiber dispersion parameters. Methods to compensate for the dispersion are also discussed.

CHAPTER 10
SYSTEM ARCHITECTURE

The system architecture is shown in Fig. (10.1). We will exam a typical broadcast-and-select network in the following chapters.

Each information bit from user *k,* denoted by b^k *(*b^k e {0,l}), is modulated (on-off key) by broadband laser pulses shaped as *s(t*). For simplicity of the denotation, we assume that *s(t)* is a rectangular pulse with a unit energy in a time slot T_c, and its frequency components cover a total bandwidth which is wide enough. The energy of *N* data bits coming out of the fcth encoder is therefore

$$w_{TX}^{k}(t) = \sum_{j=1}^{N} b^k(t - jT_c)s^k(t - jT_c)C^k \qquad t \in [0,T),\ T = NT_c \qquad (10.1).$$

where *T* is the period of the orthogonal code and *N* is the code length. The frequency hopping pattern/code is included in C^k, which obeys the rule that each wavelength at each time slot can only be assigned to one channel, as illustrated in Fig. 10.2 (a). All signals (channels) are coupled into a single mode fiber and the resulted signal is expressed by

$$w_{,,}(t) = £<(()\ \sum_{k=1}^{K} = \sum_{k=1}^{K}\sum_{j=1}^{N} b^k(t - jT_c)s^k(t - jT_c)C^k \qquad K \leq N \text{ ie}[0,T) \qquad \textbf{(10.2)}$$

The signal is broadcast to all subscribers. A decoder is installed before each optical receiver to replace the optical filter traditionally used in the optical WDM system. Mathematically, the decoder functions as a matched filter. As a result, the subscriber can conveniently change the code sequence of the decoder to select a certain channel. According to the matched code sequence that corresponds to the code in the encoder, the decoder only outputs the one selected wavelength at one time slot. Subsequently, the receiver followed transforms the signal to electronic data stream. Therefore the signal shown in Eq. (10.2) comes out the matched decoder with this form

$$>*4_{Л}»)=E_{j=1}^{N}\text{-}_{НГ}\wedge^{k(t-j} \quad ,\varepsilon[0.\Gamma) \qquad (10\_3)$$

where the factor *1/K* comes from the energy loss induced by splitter (assume the energy is distributed uniformly to each subscriber).

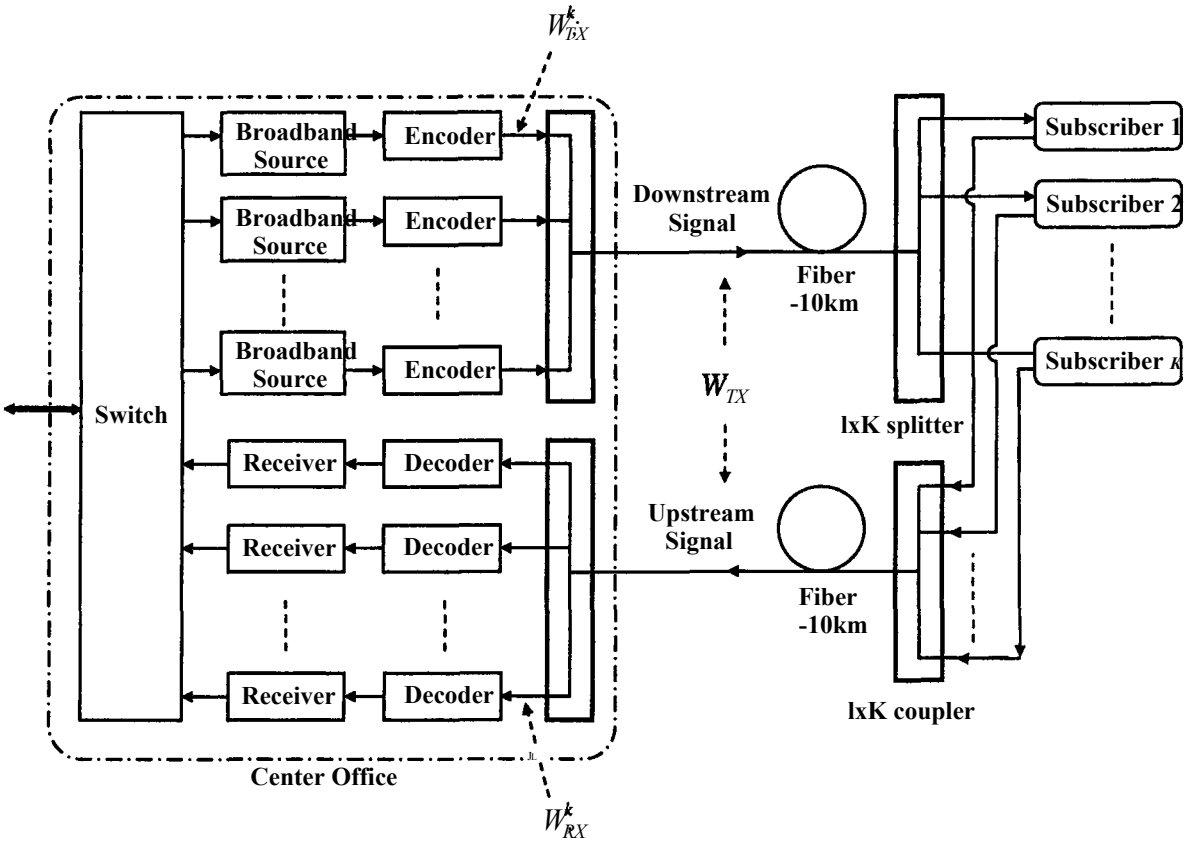

(a) System architecture

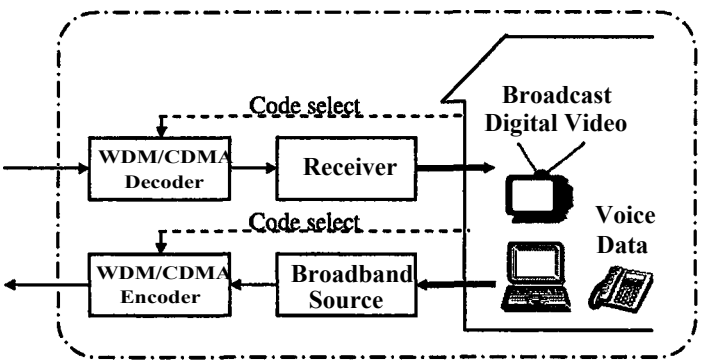

(b) Architecture of subscriber *K*

Fig. 10.1 System architecture of hybrid WDMA/CDMA

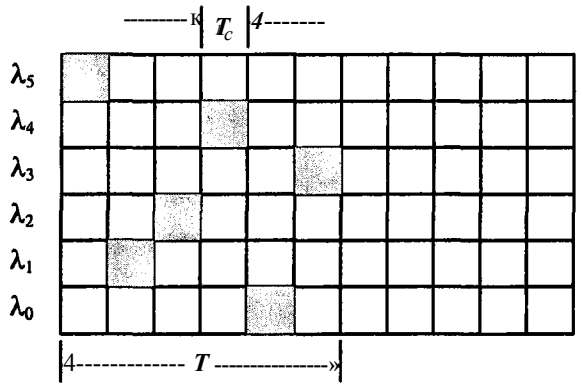

(a) Transmitted Pattern

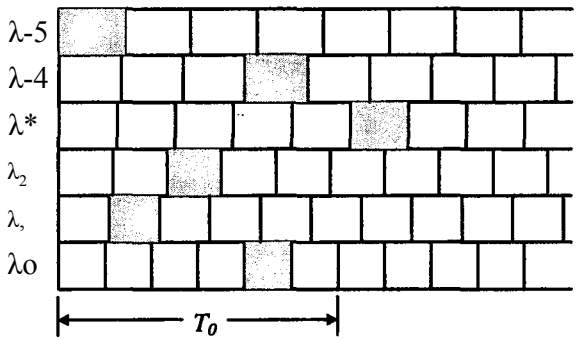

(b) Received Pattem (λ/< λ*ι)

Fig. 10.2 Wavelength-hop pattem. A filled square shows the frequency corresponding to a specific time slot. The above wavelength-hop pattern is denoted by (5,1 .гДО.3).

CHAPTER 11
MODEL OF ARRIVAL TIME DISPERSION

In this scheme, each channel is transmitted at all WDM wavelengths. Therefore, the pulses with different carrier wavelength channel, even transmitted simultaneously, arrive at the receiver asynchronously, as shown in Fig. 2(b). by referring this effect as the arrival time dispersion, which is the unique phenomenon in the hybrid of WDMA with CDMA, we will in the following. exam how the arrival time dispersion degrades the system performance.

11.1 The Parameter Q with Cross-talk

For digital communication systems, with the optimum setting of the decision threshold, the BER can be obtained by [53]

$$BER = \frac{1}{2} erfc\left(\frac{Q}{\sqrt{2}}\right) \approx \frac{\exp(-Q^2/2)}{Q\sqrt{2\pi}}$$

$$erfc(x) = \frac{2}{\sqrt{\pi}} \int_x^{\infty} \exp(-y^2) dy \qquad (11.1)$$

$$Q = \frac{I_1 - I_0}{\sigma_1 + \sigma_0}.$$

where $I_0, I_1, \sigma_0, \sigma_1$ are the means and standard deviations of the sampled values corresponding to bit 0 and 1, respectively.

We now exam the arrival time dispersion. Any practical CDMA or WDM system will suffer from cross-talk between different channels. In a specific wavelength channel, the "tails" of optical pulses in two adjacent time slots will inevitably overlap, as shown in figure (11.1). *Channel 1* is assumed to be the desired channel, thus *channel 2* and *3* are the interference. It is reasonable that we only consider the energy leaking from two adjoining bits. We assume the optical pulse is Gaussian statistics with standard deviation σ_ρ

$$P_1 = A \cdot s_p(t) = A \cdot \exp\left(-\frac{t^2}{2\sigma_p^2}\right) \tag{11.2}$$

where $s_p\ (t)$ is the pulse shape and A is its optical peak power.

Consider a PIN receiver dominated by thermal noise σ_T^* and assume the dark current is neglected. For simplicity, we assume the photo-electro transform is finished instantly and the sampling time is perfectly synchronized. Therefore the peak power $As_p(0)$ in bits

1 is related to /, as

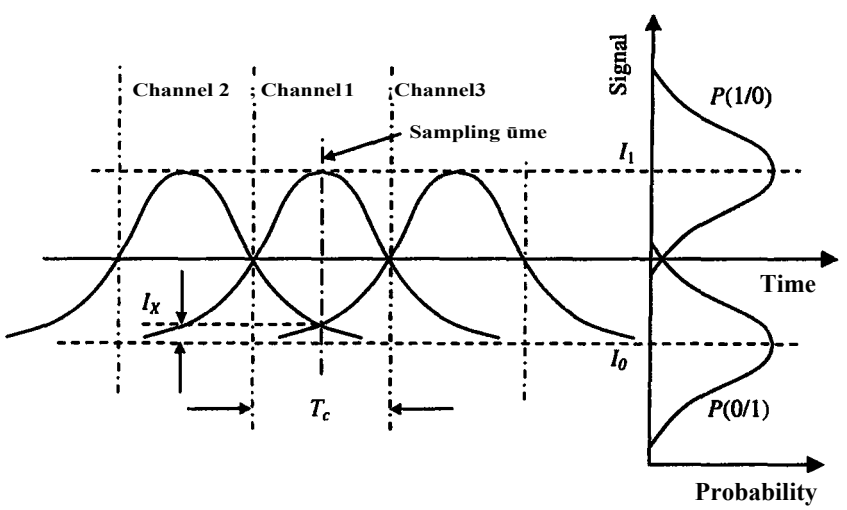

Fig. 11.1 Cross-talk in time domain at a specific wavelength channel

$$I_i = RP_l = RAs_p(0) = RA. \tag{11.3}$$

where /, is the mean value of electrical current and identical with /, in Eq. (11.1), which is perfectly sampled and only affected by thermal noise. Considering the case in which bit 0 carries no optical power so that $P_0 = 0$, i.e. /„ = 0, figure (11.1) shows that the cross-talk for bit 1 and bit 0 interacting with each other. By analyzing the figure the parameter Q in Eq.(ll.l) can be rewritten as

$$C_{v}\text{-} \frac{/\!\sim\!/\circ}{} - \frac{(I_1 + \langle I_x \rangle) - \langle I_x \rangle}{\sigma_1 + \sigma_0 \text{-} y/\emptyset\cdot,^2 \text{-} v\sigma\backslash + \text{-}J\sigma_{0^2} + \sigma^2_\chi \; 2\text{^}\sigma_\tau{}^2 + \sigma^2_\chi} = \frac{**}{} \tag{11.4}$$

where ($/_\chi$) is the mean values of cross-talk current and $\sigma\backslash$ is the variance of the random variable I_x.

To analyze the power penalty due to cross-talk, we assume *channel* 2 and *3* are equally loaded, i.e., with same bit rate, and bit 0 and 1 are transmitted with same possibility. The cross-talk power coming from two adjoining time slots will run into the desired bit with the following statistics.

Permutation of two adjoining bits	00	01 or 10	11
Cross-talk Current	0	*z	*21 χ*
Probability	1/4	1/2	1/4

Table 11.1 Statistics of two adjoining bits (without dispersion)

If the receiver and the transmitter of *channel 1* are ideally synchronized, the sampled cross-talk current for each bit 1 is equal, as shown in figure (11.1). The numerical characteristics of cross-talk current is given by

$$\begin{aligned}\langle I_x \rangle &= I_x \cdot \frac{1}{2} + 2I_x \cdot \frac{1}{4} = I_x \\ \langle I_x^2 \rangle &= I_x^2 \cdot \frac{1}{2} + (2I_x)^2 \cdot \frac{1}{4} = \frac{3}{2} I_x^2 , \\ \sigma_x^2 &= \langle I_x^2 \rangle - \langle I_x \rangle^2 = \frac{1}{2} I_x^2\end{aligned} \tag{11.5}$$

where I_x can be derived by geometry as

$$I_x = RAs_p(T_c) \longrightarrow \begin{cases} (/,) = \ddot{A}A_{Sp}(r_c) \\ \sigma_x^2 = \frac{1}{2}(RA)^2 s_p^2(T_c) \end{cases} \tag{11.6}$$

The cross-talk gives rise to the change of I_0, σ, and σ_0 in Eq.(ll.l). By combining Eqs. (11.4), (11.6) and (11.2), the parameter Q with cross-talk is derived as

$$Qx = \frac{1}{2\text{li}\hat{H}^{\wedge}} . \tag{11.7}$$

11.2 The Parameter Q with Dispersion and Cross-talk

Because each logic channel is transmitted at all WDM wavelengths, the pulses with different carrier wavelength, although transmitted simultaneously, will arrive at the receiver asynchronously. We call this effect *arrival time dispersion.* Now we exam the Q with the effect of fiber dispersion.

In fact, besides of the arrival time dispersion, each pulse is broadened (or narrows, according to its carrier wavelength) to a certain width (in time domain) at the receiver, because each pulse itself occupies certain bandwidth. Let us call this effect *pulse broadening dispersion.* We know the pulse broadening (dispersion) is proportional to the spectrum width of the pulse by [53]

$$\tau = D L \cdot A\lambda \tag{11.8}$$

where $A\lambda$ is the linewidth of the laser beam, D is the *dispersion parameter* which is a function of the carrier wavelength, and L is the fiber length. Eq.(l 1.8) is also applied for the arrival time dispersion if $A\lambda$ is the wavelength spacing between two adjoining WDM channels.

Usually, the wavelength spacing between two adjoining WDM channels is much larger than the linewidth of the laser pulse itself. Therefore, the arrival time dispersion is much more remarkable than the pulse broadening dispersion. For simplicity, we neglect the pulse broadening dispersion, i.e. assuming the shapes of all pulses are same and do not change after propagating. In this thesis, we only consider the arrival time dispersion due to the difference of central wavelengths of each WDM channel.

We denote n as the number of wavelengths used in our system. Hence, in each time slot, there are n pulses each with a different carrier wavelength, i.e. n wavelengths are used as WDM carriers. For simplicity, we assume n(>3) is odd. When n is large enough, e.g. n>10, n is odd or even does not greatly affect the precise of our analysis. We assume the sampling time is selected at the peak of the central pulse, as shown in Fig.4 (n=5, the central pulse is the 3rd). With the effect of cross-talk and dispersion, the parameter Q in Eq.(l 1.1) can be rewritten as

$$Q\ddot{a}x = \frac{h\text{-}h}{\sigma_{\chi} + \sigma_0} = \frac{\{U1d) + \langle I_{dX}\rangle) U\bar{d}x)}{4\sigma t^2 + ale + a_{ld} + \hat{}\sigma_0^2 + \sigma,} = \frac{(hd)}{\sqrt{\sigma_T^2 + \quad^2 + \quad^2 \hat{}dx} + \sqrt{\sigma_{Yd}^2 + \sigma,^2 dX}} \tag{11.9}$$

where $/_{\ddot{A}}$ is the cross-talk current when the dispersion is considered, ($/_{\text{Æ}}$) and are σ_{dX} its mean value and standard deviation, respectively. When the receiver (decoder) is ideally synchronized with the transmitter, the sampled current I_{ld} (for bit 1) fluctuates with the arrival time dispersion. Its mean value and standard deviation are ($/_{\text{ld}}$) and σ_{1d}, respectively.

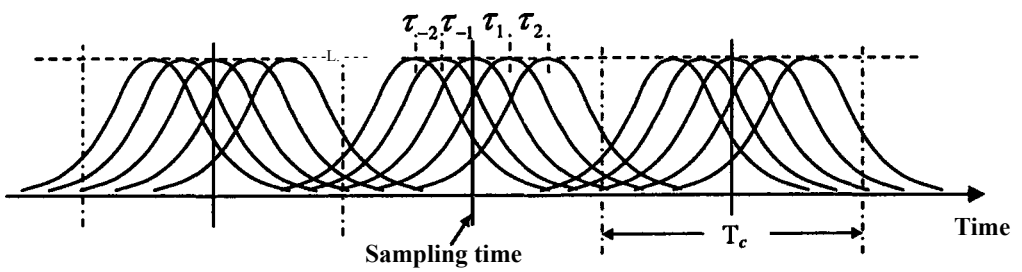

Fig. 11.2 Multi-wavelength dispersion at the receiver end

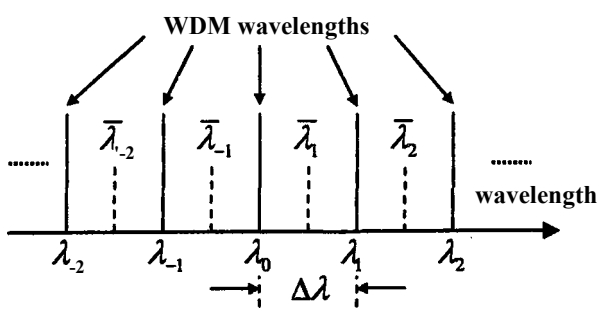

Fig. 11.3 Wavelength representation

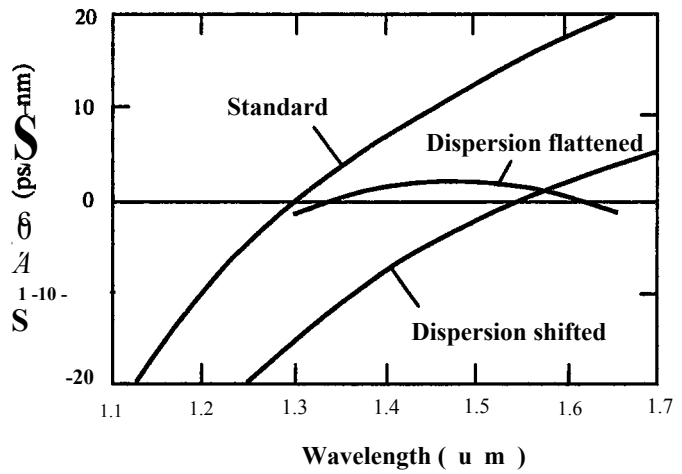

Fig. 11.4 Typical wavelength dependence of dispersion parameter D for standard, dispersion-shifted, and dispersion-flattened fibers, (from [53])

11.2.1 Analysis for Random Variance/$_{ы}$ Consider Dispersion Only

As shown in Fig. (11.3), $Л_0$ is the *central* wavelength used in this system. Ą is any of other wavelengths, where i<0 means $Ą$ < Ą and />0 means λ_i > Д,. r, is denoted as the time delay between two pulses with adjacent wavelength and in a same time slot. For instance, r, is the delay corresponding to A_0 and $Ą$, $\tau_{-\chi}$ is the delay corresponding to $Ą$ and A.J, as shown in Fig. (11.2).

We know that the pulse broadening can be calculated by Eq. (11.8), where $\Delta\lambda$ is the spectrum width of the pulse. Eq. (11.8) can be also applied to obtain the arrival time dispersion if $\acute{A}\tilde{A}$ is the wavelength spacing between two adjoining WDM channels. Now we want to know the time delay $т$, between two pulses with carrier wavelengths $Ą$ and /t_w, respectively. This problem equals to how much a *virtual pulse*. which is at a carrier wavelength $\bar{A_i}$ = (Л, + Л$_{1ч}$)/2 and with a spectrum width [$Л._{-\chi}$, $Л_{\chi}$], will spread after

propagating in the fiber, as shown in Fig. (11.3). We assume A_j is selected with equal wavelength spacing $A\lambda = A_j \sim\lambda_M$. Thereby the dispersion r_j for a fiber with length L can be written as

$$\tau_{i} = D_{i} \cdot LAA \tag{11.10}$$

where D_i is the *dispersion parameter* for each WDM wavelength. With current technology, $A\lambda$ is typically with the order of ~1 nm and n is usually not more than 100, i.e. the wavelength is within the range of 0.1 pm. Therefore, with the reference of Fig.(11.4), the dispersion parameter can be linearly approximated by

$$D_i = d(\lambda_i - \lambda_{20}) = \begin{cases} d\lambda_Q + (i-0.5)A\lambda A_m & i = 1,2,\cdots,(n-1)/2 \\ d[\lambda_0 + (i+0.5)AA - AJ & i = -1,-2,\cdots,-(n-1)/2 \end{cases} \tag{11.11}$$

where d is the group velocity dispersion slope [ps/(km*nm^2)], and A_m is the zero-dispersion wavelength, depending on the fiber characteristics.

By analyzing Fig.(l 1.2), (l_{xd}) and $(l_{Xd}$ can be written as

$$\begin{aligned} \{h\ddot{a}\} &= \frac{RA}{n}\left[s_p\{\tau_{-2}+\} + \tau_{-1} s_p(\mathbf{r}_{-1}) + s_p(0)\cdot + \mathbf{i}_1(\mathbf{r}_1)\blacksquare + \mathbf{j}_1(\mathbf{r}_1 + \tau_2) + \cdots \right] \\ &= \frac{RA}{n}\left\{ s_p(0) + \sum_{i=1}^{(n-1)/2}\left[s_p\left(\sum_{j=1}^{i} I s_j \right) + s_p\left(\sum_{VM} \right) \right] \right\} \\ &= \frac{RA}{n}\left\{ s_p(0) + \sum_{i=1}^{(n-1)/2}\left[s_p\left(\sum_{j=1}^{i} LAA \cdot Dj \right) + s_p\left(\sum_{j=1}^{i} L\cdot AA \cdot D_j \right) \right] \right\} \\ &= RAS_X \end{aligned} \tag{11.12a}$$

$$\{Ч) = \text{^-}\backslash\text{-} + \text{ф-1+u)} + \text{^-} \text{,)+ị(0)+ịW} + \text{^fc+*-2)} + \cdots]$$

$$= \frac{\mathbf{M1}}{n} \left\{ \text{*^(°)} + \sum_{i=1}^{(n-D/2)} \left[\cdot \right\} \left(\sum_{j=1}^{\cdot} \right) \right] + s_p^2 \left| \sum^{(i\ \lambda} \text{*} \cdot \right| \right\} \quad (11.12b)$$

$$= \frac{RA}{n} \left\{ s_{t,}^{2} (\text{»}) + \sum_{i=1}^{(n-1)/2} \left[s_p^2 \left(L\text{-}MY, \ D\ J \right| + 5_p^2 \left(LAX\text{^}D.J \right) \right] \right\}$$

$$= (RAfS,$$

where

$$Si\text{-}_{tt} \left\{ \sum_{i=-(B-1)/2}^{(B-1)/2} \left[s_p \left(LAX\text{^}DJ \right) \right] \right\}$$

$$S_2 = \frac{1}{n} \left\{ \sum_{i=-(B-1)/2}^{(B-D/2} \left[s_p^2 \left(LAX\text{^}DJ \right) \right] \right\}$$

and define $D_0 = 0$ (no physical meaning). S_1 and S_2 can be termed as *normalized 1st and 2fid moment of sampled value,* respectively, independent on photo-electric converter and the peak value of the pulse. Then, the variation is gotten by

$$\text{of, =(',/)-<!,л}^2 = (\text{ÄA})'(S_2 - S.^2) \quad (111\text{-}3)$$

11.2.2 Analysis for Random Variance I_{dX} Consider Dispersion and Cross-talk

Compared to the case neglecting the effect of dispersion, the power of cross-talk coming from the *left* adjoining time slot will increase, while the power of cross-talk coming from the *right* time slot will decrease, as shown in Fig. (11.5).

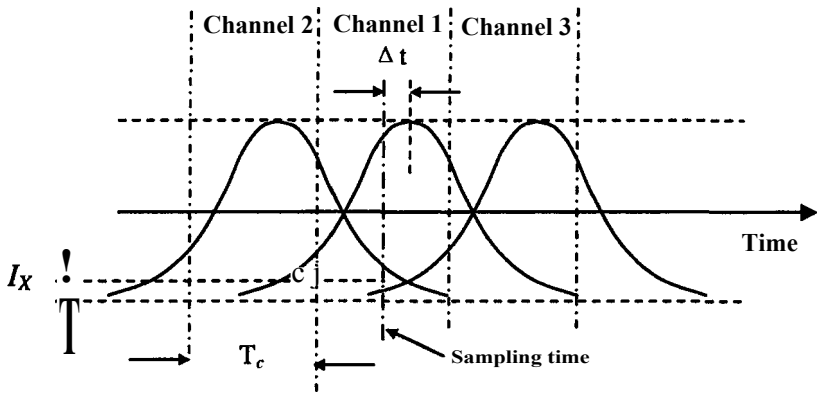

Fig. 11.5 Cross-talk with dispersion
(Only one wavelength channel is shown.)

Permutation of two adjoining bits	**00**	**01**	**10**	**11**
Cross-talk Current	**0**	$\int_{T}^{(R)} dX$	**z a.)** $\int dX$	$\int_{}^{j(L)} + \int_{T}^{j(R)} dX$
Probability	**1/4**	**1/4**	**1/4**	**1/4**

Table 11.2 Statistics of two adjoining bits (with dispersion)

Firstly, we only consider one wavelength channel. This effect changes I_x of Eq.(7) into two different cross-talk currents (one from the *left,* the other from the *right),* denoted by

$$\begin{aligned} I_{P}^{(L)} &= RAs\,(T_r - At) \\ I^{\wedge} &= RAs_p(T_c + At) \end{aligned} \qquad (11.14)$$

Therefore, the statistics in Table (11.1) should be rewritten by Table (11.2). Then, the numerical characteristics of cross-talk current can be obtained by

$$\langle I_{dX} \rangle = \frac{1}{2}\left(I_{dX}^{(L)} + I_{dX}^{(R)}\right) = \frac{RA}{2}\left(s_p(T_c - \Delta t) + s_p(T_c + \Delta t)\right)$$
$$= \frac{RA}{2}\left\{\exp\left[-\frac{\text{fc-}\Delta\text{»})^2]}{2\sigma I \ \backslash}\right] + \exp\left[-\frac{(T_V + \grave{a}tf]}{\text{L } 2\sigma I \text{ Jj}}\right]\right\} \quad (11.15a)$$

$$\wedge = (\iota^2 A - (\iota * Y = \frac{1}{4}\left(I_{dX}^{(L)2} + > £)^2\right)$$
$$= \frac{(RA)^2}{4}\left\{\exp\left[-\frac{\text{fc-}\Delta\acute{\imath})^2}{\sigma_p^2}\right] + \exp\left[-\frac{(\Gamma, + \Delta/)^2}{\sigma_p^2}\right]\right\} \quad (11.15b)$$

In any system with accepted performance, $At \ll T_c$ is always satisfied. Thereby Eq.(11.15) can be approximated by

$$(1_{л}) \text{-} Я Л a p \text{ --} \left[\frac{T^2}{2\sigma_{B_{pj}}} - RA s_p \hat{I} T_c\right) = 1_x = </,) \quad (11.16a)$$

$$\sigma \grave{\alpha} X \tilde{} \frac{(RA)^2}{2} \blacksquare \exp\left(-\frac{(rj\%2\wedge}{\sigma_p}\right) = \frac{1}{2}\left[RA s_p(T_c)\right]^2 = \frac{1}{2} I_X^2 = \sigma_X^2 . \quad (11.16b)$$

By combining Eqs.(11.9), (11.12a), (11.13) and (11.16b), the parameter Q with dispersion and cross-talk can be given by

$$a, = \frac{\underline{RAS.}}{\wedge(T\tau + {}^2(T\chi + {}^2(\lambda\alpha)\,(\text{iS}_2^2 - Sy\,\text{j} + {}^2\wedge(TT + \sigma\backslash\,{}^2}$$
$$= \frac{Si}{\sqrt{\left(\frac{\sigma_T}{RA}\right)^2 + \frac{1}{2}s_p^2(T_c) + (S_2 - S_1^2)} + \sqrt{\left(\frac{\sigma_T}{RA}\right)^2 + \frac{1}{2}s_p^2(T_c)}} \quad (11.17)$$

11.3 Power Penalty due to Dispersion

We use *power penalty* to describe the deterioration of system performance, which is defined by

$$J = 10\log_{10}\left(\frac{\overline{P}_{rec}(disp. + cros.)}{\overline{P}_{rec}(CrOS\cdot)}\right) \tag{11.18}$$

where $\overline{P}_{rec}$ is the average received power, which is defined as $\overline{P}_{rec} = (P_Q + P_i)/2$, P_0 and Pi is the received (sampled) power, corresponding to bit 0 and 1, respectively. $\overline{P}_{rec}(cros.)$ is the average received power when dispersion is not considered and only the crosstalk is considered, while $\overline{P}_{rec}$ (*disp. + cros.)* is the average received power when both dispersion and crosstalk are considered. The power penalty means, when the system is degenerated by some reason(s) (in our case, the reason is dispersion), the system can keep the same bit-error-rate (or *Q)* only if the received average power is increased by δ dB by means of increasing the transmission power.

Now we consider the situation only with cross-talk. By the definition and combining Eq.(l 1.5) and (11.6), the average received (sampled) power is gotten by

$$\overline{P}_{rec(CrOS\cdot)} = \frac{P_0 + P_1}{2} = \frac{1}{2}\left[\frac{\langle I_X\rangle}{R} + \left(\frac{\langle I_X\rangle}{R} + A\right)\right] = A\left(\frac{1}{2} + \delta(r_c)\right). \tag{11.19}$$

By combining Eq.(11.7) with Eq.(11.19) and deleting *A,* we get

$$\overline{P}_{jeras.}) = \frac{2Q\sigma_T}{R}\left(\frac{1}{2} + \delta(T,)\right)(1 - 2\beta^J \, fa)). \tag{11.20}$$

Now we consider the situation with both dispersion and cross-talk. By the definition and combining Eq.(l 1.12a) with Eq.(l 1.16a), the average received (sampled) power is gotten by

$$\overline{Prec}\ (<disp.+cros.) = \wedge [(f_{\ddot{A}}) + ((/_{д}) + (Z_w >)] := A\acute{I}\ S_P\{T_c) + \left(\frac{S_1}{2}\right). \tag{11.21}$$

By combining Eq.(11.17) with Eq.(11.21) and deleting *A,* we get

$$\overline{P}_{rec}(disp.+cros.) = \frac{2Q\sigma_T}{R}\left(\frac{P}{V_z}\right)^{S}\mathbb{M} \qquad \left[\left(\left(\frac{V_A}{4U.}\right)\left(\frac{S_2}{J}-S_1\right)Q^2\text{-}s,\right)^{N^2} \text{-}2\ Q^2 s^2{}_p\{T_c)\right]^{\frac{1}{2}} \tag{11.22}$$

Finally, the power penalty can be gotten by combining Eqs.(11.18), (11.20) and (11.22) as

$$\delta = 5\log\frac{\left(\frac{S_1}{2}+s_p(T_c)\right)^2\left(1-2Q^2s_p^2(T_c)\right)}{\left(\frac{1}{2}+s_p(T_c)\right)^2\left[\left(\left(\frac{S_2}{S_1}-S_1\right)Q^2-S_1\right)^2-2Q^2s_p^2(T_c)\right]}. \tag{11.23}$$

CHAPTER 12
SIMULATION AND DISCUSSION

12.1 Model Implementation

If the non-retum-to-zero code format is employed, the bit rate and pulse width can be set by $B = 1/T_c = 1/2.5\sigma_p$ [52]. Therefore, the Gaussian pulse can be written by

$$s_p(\mathrm{i}) = \exp\left(\frac{t^2}{2\sigma_p}\right) = \exp(-3\beta V) \qquad (12.1)$$

$$^{\wedge}{}_{P(7'c)} = \exp(-3)$$

Combining Eqs.(l 1.12a), (11.12b) and (12.1), we have

$$S_{,} = \frac{1}{n}\left\{\sum_{i=-(n-1)/2}^{(n-1)/2}\left[\exp\left(-3\left(\frac{i}{BLAX^{\wedge}Dj}\right)^{2^{\wedge}}\right)\right]\right\} \qquad (12.2)$$

$$s_2 = \frac{1}{n}\left\{\sum_{i=-(n-1)/2}^{(n-1)/2}\left[\exp\left(-6\left(\frac{i}{BLAA^{\wedge}Dj}\right)^{2^{V}}\right)\right]\right\}$$

With previous analysis the dispersion parameter is given by

$$D_i = d(\bar{A}_i - \Pi_m) = \begin{cases} d[\ddot{A}_0 + (i - 0.5)\Delta\lambda - \lambda\hat{}] & (/= 1,2,\cdots,(\eta - 1)/2) \\ O & (i = 0) \\ \acute{\alpha}[\lambda o + (i + 0.5)\Delta\Lambda - \lambda\eta\ ] & (i = -1,-2,\cdots,-(\eta - 1)/2) \end{cases} \quad (12.3)$$

The parameters d and λ_{ZD} are the characteristics of the fiber. For the conventional single mode fiber (e.g. Coming SMF-DS, see page 44 of [53]), as shown in Fig. (11.4), the value are d = 0.075 [ps/(km*nm^2)], λ_{ZD} = 1550 [nm]. The central wavelength of WDM is Π_0 = 1552.524 [nm] and wavelength spacing $\acute{A}\tilde{A}$ = 0.8034 [nm] (i.e. Af = 100 [GHz]). With above parameters, the simulation result of Eq. (11.23) is shown in Fig. (12.1). Fig. (12.2) is the simulation result with three different wavelength spacing $Af_{\cdot}$ = 200 [GHz], Af = 100 [GHz] and Af = 50 [GHz]. Fig.(12.3) is the simulation result with four kinds of fibers, as shown in Table (12.1).

12.2 Result Discussion

Eq. (11.23) provide a simple, yet insightful analytical expression for calculating the system performance degeneration due to fiber dispersion in the hybrid of frequency-hopping optical CDMA and WDMA system as a function of the system capacity (measured by the product of the bit rate B and the distance L) and the number of total subscribers n. Due to the fiber dispersion, it is noted that the maximum system capacity and the number of subscribers are limited as shown in Fig. (12.1). In order to find some approaches to compensate the degeneration, we analyze some other parameters, which also affect the power penalty.

(1) WDM wavelength spacing.

The total wavelength span of the system depends on the WDM wavelength spacing of each channel. The narrower the wavelength spacing is, the better the

system performs, as shown in Fig. (12.2). Thereby, one approach to improve the system performance is to employ the narrower wavelength spacing.

(2) Dispersion parameter of the fiber.

Different dispersion parameteres of the fiber will leads to different power penalties, as shown in Fig. (12.3). The less difference between the zero-dispersion wavelength and the system central wavelength λ_0 , and/or, the less slop of the group velocity dispersion, the better the system can perform. Thereby, to employ fibers with proper dispersion parameter is also an approach to improve the system performance.

It should be noted that the above two methods can only improve the system performance to a limited extent. Present WDMA systems can work with a bit-rate distance product of the order of several hundred (Tb/s)*km [53] in long haul systems. But Figs. (12.1), (12.2) and (12.3) show us that the hybrid system of WDMA and FP-CDMA can work with the bandwidth*distance on the order of several hundred (Gb/s)*km only. The reason of so much difference is that this scheme requires a wavelength span equal to that of the WDMA system and the synchronization among all the wavelength channels is involved, whereas there is not such synchronization in WDMA systems.

If the WDMA/CDMA frequency hopping system works with a large bit-rate distance product, the optical decoder must be able to compensate the arrival time dispersion according to the fiber length. That is to say that the extent of dispersion compensation of must be adjustable according to the fiber length. Nevertheless, if the product of bit rate and distance is small enough so that the power penalty is acceptable, this dispersion compensation can be waived. Whether the dispersion compensation is required or not can be estimated by Eq. (11.23).

After the arrival time dispersion is properly compensated, the *pulse broadening dispersion* is the main factor for the deterioration of system performance. The reason is that the pulses with different carrier frequencies experience different dispersion so that the arrival pulses have different peak value. Therefore, the power penalty characterized by Eq. (11.23) is just an optimistic estimation, which does not cover the degeneration due to the *pulse broadening dispersion.*

In summary, the hybrid of WDMA/CDMA frequency hopping system does suffer serious performance deterioration due to the fiber dispersion. But that can be compensated in a certain degree and may not be a serious problem in local area networks, in which it offers an attractive multi-access approach.

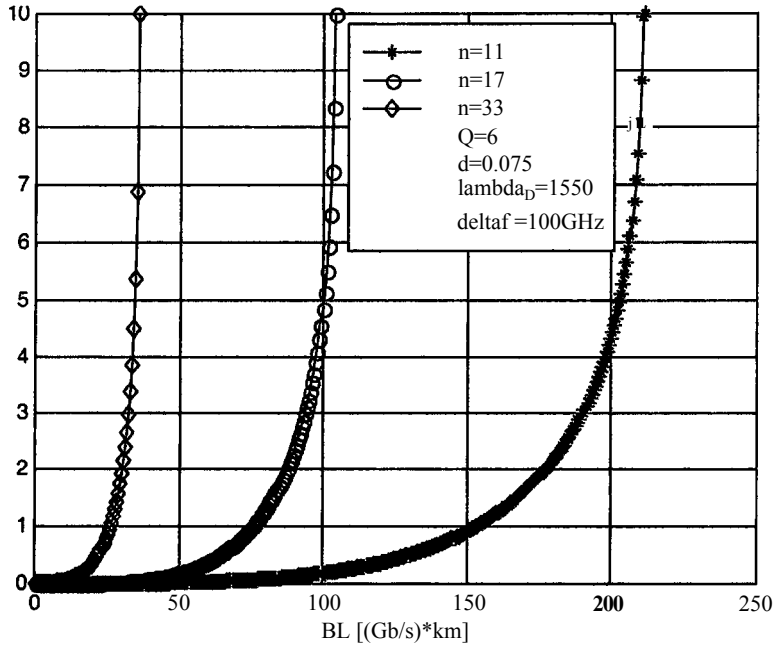

Fig. 12.1 Power penalty with different wavelength number

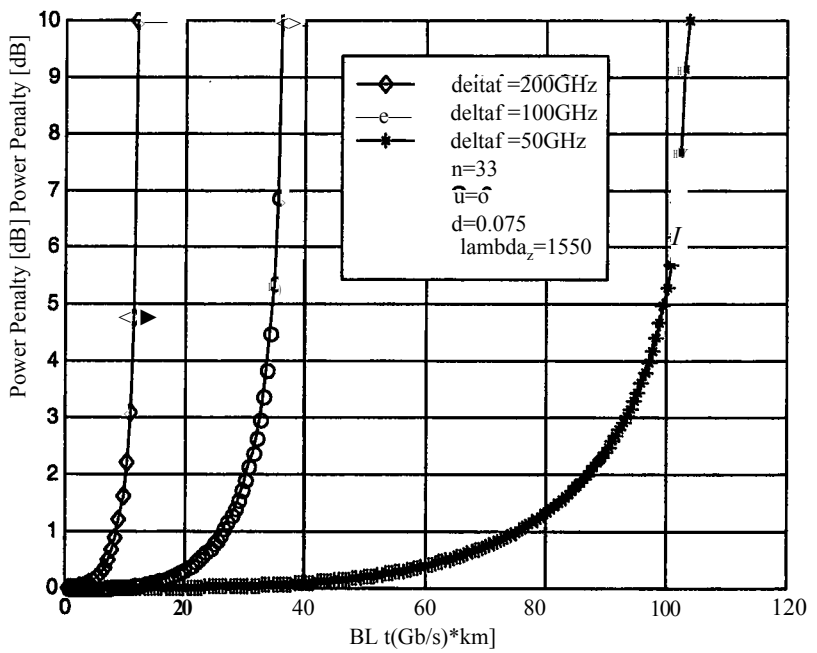

Fig. 12.2 Power penalty with different wavelength spacing

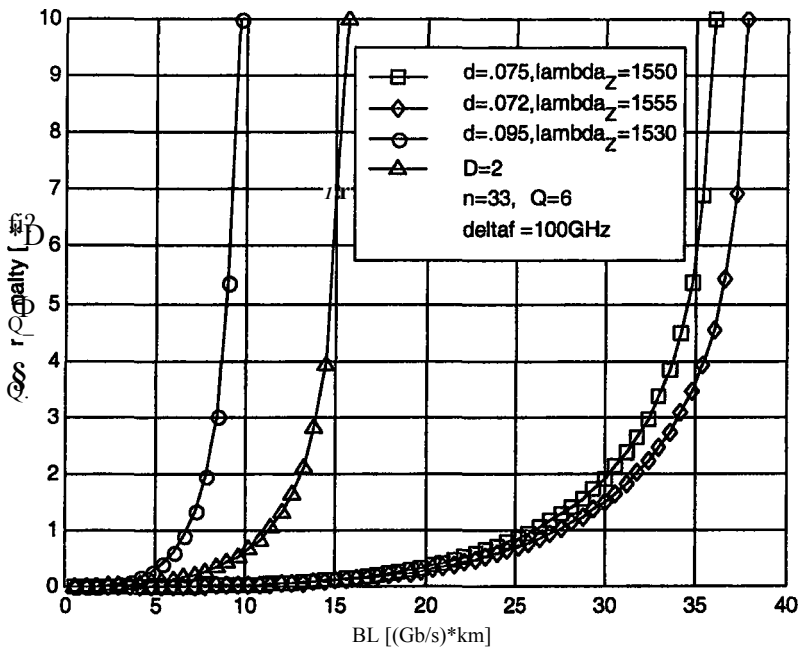

Fig. 12.3 Power penalty with different dispersion parameter

Parameters	Coming SMF-DS	L1TESPEC DSM-15	AT&T TrueWave	Flattened fiber
GVD slop d [ps/km*nm^2]	0.075	0.072	0.095	0 (assume D =2)
λ_{ZD} [nm]	1550	1555	1530	-

Table 12.1 Dispersion parameters of different fibers

APPENDIX
SIMULATION PARAMETERS

1. SOA Structure Parameters *

L_a	Length of active region (FP-SOA and DBR-SOA) ($\mu\chi\eta$)	600
L_{DBR}	Length of DBR region in DBR-SOA ($\mu\chi\eta$)	200
d	Depth of active region (//m)	0.2
w	Width of active region ($\mu\chi\eta$)	1.2
κ	Coupling coefficient of Bragg grating	600
Γ	Optical confinement factor	0.45
Rj, R_2	Reflectivity of facet (both ends, FP-SOA and DBR-SOA)	5 x 10"5
/7,, η_2	Fiber-SOA coupling loss at both ends (dB)	3

2. Working Parameters (Except for Denoted)

$Л_ш$	Input signal wavelength (nm)	1550
Λβι	Lasing wavelength (nm)	1530
I_{FP}	Bias current of FP-SOA (mA)	80
I_{DBR}	Bias current of DBR-SOA (mA)	200

3. Non-physical Simulation Parameters

K_d	Frequency discretizaiton factor	12
(N.A.)	Simulated ASE bandwidth (nm)	1490~1590
(N.A.)	Section number of active region in FP-SOA	120
(N.A.)	Section number of active region in DBR-SOA	120
(N.A.)	Section number of DBR region in DBR-SOA	40

4. Material Parameters

K_0	Carrier independent absorption loss coefficient (m^{-1})	3000
σ_1	Carrier independent absorption loss coefficient (m^2)	7500 xlO"24
A_{nrad}	Linear nonradiative recombination coefficient (s^{-1})	3.6x10®
B_{nrad}	Bimolecular nonradiative recombination coefficient (m^3/s)	5.6x 10 -16
c_{aug}	Auger recombination coefficient (m^6/s)	3x10^'
A_{rad}	Linear radiative recombination coefficient (s^{-1})	l.OxlO7
B_{rad}	Bimolecular radiative recombination coefficient (m^3/s)	5.6 xlO"16
n_s	Effective group refractive index	4.1798
n_{eff0}	Effective index at reference carrier density and frequency	3.5
$\frac{dn_{eff}}{dv}$	Linear coefficient of index verse frequency (1/Hz)	4×H-10
$\frac{dn_{eff}}{dN}$	Linear coefficient of index verse carrier density (m^3)	-1.33 x IO-26
N_0	Reference carrier density (m^{-3})	1.5x1o24
V_O	Reference frequency (Hz)	1.9986 xlO14
a	Bandgap energy quadratic coefficient	1.35
b	Bandgap energy quadratic coefficient	-0.775

c	Bandgap energy quadratic coefficient	0.149
K_g	Bandgap shrinkage coefficient (eVm)	0.9 xlO^{-10}
T	Absolute temperature (Kelvin)	300
m_e	Effective mass of electron in the CB (kg)	4.1 xlO^{-32}
m_{hh}	Effective mass of a heavy hole in the VB (kg)	4.19 xlO^{-31}
m_{bl}	Effective mass of a light hole in the VB (kg)	5.06 xlO^{-32}

BIBLIOGRAPHY

[1] N. Savage, "Linking with light," *IEEE Spectrum,* vol. 39, pp.32-36, August 2002.

[2] M. J. O'Mahony, "Semiconductor laser optical amplifiers for use in future fiber systems," *IEEE J. Lightwave Technology,* vol. 6, pp. 531-544, April 1988.

[3] A. J. Lowery, "Computer-aided photonics design," *IEEE Spectrum,* vol. 34, pp.26-31, April 1997.

[4] C. F. Tsang, D. D. Marcenac, J. E. Carroll, L. M. Zhang, "Comparison between 'power matrix model' and 'time domain model' in modelling large signal responses of DFB lasers," IIIE Proceedings, Optoelectronics, vol. 141, pp. 89-96, April 1994.

[5] M. A. Summerfield, R. S. Tucker, "Frequency-domain model of multiwave mixing in bulk semiconductor optical amplifiers," IEEE J. Selected Topics in Quantum Electronics, vol. 5, pp. 839 -850, May-June 1999.

[6] D. Cassioli, S. Scotti, A. Mecozzi, "A time-domain computer simulator of the nonlinear response of semiconductor optical amplifiers," IEEE J. Quantum Electronics, vol. 36, pp. 1072 -1080, Sept. 2000.

[7] R. Gutierrez-Castrejon, L. Schares, etc. "Modeling and measurement of longitudinal gain dynamics in saturated semiconductor optical amplifiers of different length," IEEE J. Quantum Electronics, vol. 36, pp. 1476 -1484, Dec. 2000.

[8] M. J. Connelly, "Wideband semiconductor optical amplifier steady-state numerical model," IEEE J. Quantum Electronics, vol. 37, pp. 439 - 447, March 2001.

[9] M. J. Connelly, "Wideband dynamic numerical model of a tapered buried ridge stripe semiconductor optical amplifier gate," TEE Proceedings, Circuits, Devices and Systems, vol. 149, pp. 173 - 178, June 2002.

[10] J. Park, X. Li, W.P. Huang, "Performance simulation and design optimization of gain-clamped semiconductor optical amplifiers based on distributed Bragg reflectors," IEEE J. Quantum Electronics, vol. 39, pp. 1415-1423, November 2003.

[11] R.G. Smith, "Optical power handling capacity of low loss optical fibers as determined by stimulated Raman and Brillouin Scattering," Applied Optics, vol. 11, pp. 2489 - 2494, November 1972.

[12] D. Cotter, "Observation of stimulated Brillouin scattering in low-loss silica fiber at 1.3pm," Electronics Letters, vol. 18, pp. 495 - 496, June 1982.

[13] R.H. Stolen and E.P. Ippen, "Raman gain in glass optical waveguides," Applied Physics Letters, vol. 22, pp. 276 - 278, March 1973.

[14] E. Desurvire, Erbium Doped Fiber Amplifiers: Principles and Applications, New York: John Wiley & Sons, 1994.

[15] Zhaohui Zheng and Xun Li, "Simulation of erbium-doped fiber amplifier based on a novel dynamic model", Master Thesis in McMaster University, 2002.

[16] A. Reale, A. Di Carlo, P. Lugli, "Gain dynamics in traveling-wave semiconductor optical amplifiers," IEEE Selected Topics in Quantum Electronics, vol. 7, pp. 293-299, March-April 2001.

[17] D.T. Schaafsma, E.M. Bradley, "Cross-gain modulation and frequency conversion crosstalk effects in 1550nm gain-clamped semiconductor optical amplifiers," IEEE, Photonics Technology Letters, vol. 11,6, pp. 727 - 729, June 1999.

[18] D.T. Schaafsma, E. Miles, E.M. Bradley, "Comparison of conventional and gain-clamped semiconductor optical amplifiers for wavelength-division-multiplexed transmission systems," IEEE J. Lightwave Technology, vol. 18, pp. 922 - 925, July **2000.**

[19] T. Durhuus, B. Mikkelsen, etc., "All-optical wavelength conversion by semiconductor optical amplifiers," IEEE J. Lightwave Technology, vol. 14, pp. 942 - 954, June 1996.

[20] M. Asghari, I. H. White, R. V. Penty, "Wavelength conversion using semiconductor optical amplifiers," IEEE J. Lightwave Technology, vol. 15, pp. 1181 -1190, July 1997.

[21] B. Bauer, F. Henry, R. Schimpe, "Gain stabilization of a semiconductor optical amplifier by distributed feedback," IEEE Photonics Technology Letters, vol. 6, pp. 182-185, Feb. 1994.

[22] M. Bachmann, P. Doussiere, etc., "Polarisation-insensitive clamped-gain SOA with integrated spot-size convertor and DBR gratings for WDM applications at 1.55 pm wavelength," IEEE Electronics Letters, vol. 32, Iss, 22, pp. 2076-2078, Oct. 1996.

[23] Shyh Wang, "Principles of distributed feedback and distributed Bragg-reflector lasers," IEEE J. Quantum Electronics, vol. 10, pp. 413-427, April 1974.

[24] G..P. Agrawal, N.K. Dutta, Semiconductor Laser (second ed.), Van Nostrand Reinhold.

[25] S. J. B. Yoo, "Wavelength conversion technologies for WDM network applications," IEEE J. Lightwave Technology, vol. 14, pp. 955-966, June 1996.

[26] G.P. Agrawal, I.M.I. Habbab, "Effect of a four-wave mixing on multichannel amplification in semiconductor laser amplifiers," IEEE J. Quantum Electronics, vol. 26, pp. 501 - 505, March 1990.

[27] F. Favre, D. Guen, "Four-wave mixing in traveling-wave semiconductor laser amplifiers," IEEE J. Quantum Electronics, vol. 26, pp. 858 - 864, May 1990.

[28] A. Mecozzi, S. Scotti, etc., "Four-wave mixing in traveling-wave semiconductor amplifiers," IEEE J. Quantum Electronics, vol. 31, pp. 689 - 699, April 1995.

[29] Dubovitsky, S.; Steier, W.H, 'Tunable wavelength filters based on nonlinear optical interactions in semiconductor amplifiers," IEEE J. Lightwave Technology, vol. 14, pp. 1020 - 1026, June 1996.

[30] J.H. Kim, K.R. Oh, etc. "All-optical switching by counterpropagating operation in cascaded semiconductor optical amplifiers," IEEE Photonics Technology Letters, vol. 12, pp. 513 - 515, May 2000.

[31] K. Vyrsokinos, G. Toptchiyski, K. Petermann, "Comparison of gain clamped and conventional semiconductor optical amplifiers for fast all-optical switching," IIIEE J. Lightwave Technology, vol. 20, pp. 1839 - 1846, Oct. 2002.

[32] K.E. Stubkjaer, "Semiconductor optical amplifier-based all-optical gates for high-speed optical processing," IEEE J. Selected Topics in Quantum Electronics, vol. 6, pp. 1428-1435, Nov.-Dee. 2000.

[33] A. Hamie, A. Sharaiha, etc. "All-optical logic NOR gate using two-cascaded semiconductor optical amplifiers," IEEE Photonics Technology Letters, vol. 14, pp. 1439 -1441, Oct. 2002.

[34] J.H. Kim, Y.M. Jhon, etc., "All-optical XOR gate using semiconductor optical amplifiers without additional input beam," IEEE Photonics Technology Letters, vol. 14, pp. 1436 - 1438, Oct. 2002.

[35] R. Olshansky, C. A. Su, J. Manning, and W. Powazinik, "Measurement of radiative and nonradiative recombination rates in InGaAsP and AlGaAs light sources," IEEE J. Quantum Electronics, vol. QE-20, pp. 838-854,1984.

[36] M. Kot and K. Zdansky, "Measurement of radiative and nonradiative recombination rate in InGaAsP-InP LED's," IEEE J. Quantum Electronics, vol. 28, pp. 1746-1750, 1992.

[37] N. G. Nilsson, "Empirical approximations for the fermi energy of a semiconductor with parabolic bands," Applied Physics Letters, vol. 33, pp.653-654,1978.

[38] Govind P. Agrawal, "Fiber-Optic communication Systems (second ed.)", John Wiley & Sons, INC., 1997.

[39] K. Petermann, "Calculated spontaneous emission factor for double heterostructure injection lasers with gain induced mode guiding," IEEE J. Quantum Electron., vol. QE-15, pp. 566-570,1979.

[40] L.M. Zhang, S. F. Yu, etc. "Dynamic analysis of radiation and side-mode suppression in a second-order DFB laser using time-domain large-signal traveling wave model," IEEE J. Quantum Electronics, vol. 30, pp. 1389 - 1395, June 1994.

[41] W. Lá, W.P. Huang, X. Li, J. M. Hong, "Multiwavelength gain-coupled DFB laser cascade: design modeling and simulation," IEEE J. Quantum Electronics, vol. 36, pp. 1110-1116, October, 2001.

[42] D. M. Pozar, Microwave Engineering. New York: Wiley, 1998.

[43] C. A. Brackett, "Dense Wavelength Division Multiplexing Networks: Principles and Applications", IIIEE, Journal on Selected areas in Comm., Vol.8, pp.948, Aug. 1990

[44] V. K. Jain, G. D. Marchis, "Hybrid Wavelength and Code Division Multiple Access in Optical Networks", Fiber and Integrated Optics, 20:1-19,2001.

[45] J. A. Salehi, "Code division multiple-access techniques in optical fiber networks — Part I: Fundamental principles", IEEE Trans. Commun., vol.37, pp. 824-833, Aug. 1989.

[46] J. A. Salehi and C. A. Brackett, "Code division multiple-access techniques in optical fiber networks — Part II: Systems performance analysis ", IIIEE Trans. Commun., vol. 37, pp. 834-842, Aug. 1989.

[47] F. R. K. Chung, J.A. Salehi, etc. "Optical orthogonal codes: Design, analysis, and applications", IIIEE Trans. Inform. Theory, vol. IT-35, pp. 595-604, May. 1989.

[48] H. Fathallah, L. A. Rusch, S. LaRochelle, "Passive Optical Fast Frequency-Hop CDMA Communicaitons System", J. Lightwave Tech. Vol. 17, pp. 397, Mar. 1999.

[49] R. M. Gagliardi, A. J. Mendez, etc. "Fiber-optic digital video multiplexing using optical CDMA", J. Lightwave Technol., vol. 11, pp. 20-26, Jan. 1993

[50] K. Sato, T. Ohtsuki, H. Uehara, I. Sasase, "Effect of imperfect slot synchronization on derect-detection optical synchronous CDMA Communication Systems with PPM signaling", J. Lightwave Technol., Vol. 14, pp. 1963, Sep.1996

[51] J. J. O'Reilly, J.R.F. da Rocha, K. Schumacher, "Influence of timing errors in the performance of direct-detection optical-fiber communication systems", IIIE PROCEEDINGS, Vol. 132, PtJ, pp.309, Oct. 1985

[52] K. Schumacher, J.J. O'Reilly, "Power penalty due to jitter on optical communication systems", Electronics Letters, 11th, May 1987

[53] G. P. Agrawal, Fiber-Optical Communication Systems, 2nd Edition, John Wiley & Sons. Inc., 1997.

[54] G. P. Agrawal, Nonlinear Fiber Optics, 2nd Edition, Academic Press Inc., 1995.

[55] J. M. Senior, Optical Fiber Communications Principles and Practice, 2nd Edition, Prentice Hall Ltd., 1992.